

# **Quantitative Magnetic Resonance Imaging in experimental and applied clinical research**

**Ph.D. thesis**

**Mihály Aradi, M.D.**

**University of Pécs**

**2013.**

**Supervisor: Attila Schwarcz, M.D., Ph.D.**



## TABLE OF CONTENT

<b>Acknowledgements</b> .....	3
<b>Abbreviations</b> .....	4
<b>I. Introduction</b>	
1. Preface.....	5
2. Basics of NMR-MRI.....	6
3. The way to MR Imaging.....	8
4. Qualitative Imaging.....	8
5. Quantitative Imaging.....	10
<b>II. Quantitative proton MRI and MRS of the rat brain with a 3 T clinical MR scanner</b>	
1. Introduction.....	11
2. Materials and Methods.....	13
3. Results.....	19
4. Discussion.....	23
<b>III. Quantitative MRI studies of chronic brain white matter hyperintensities in migraine patients</b>	
1. Introduction.....	28
2. Materials and Methods.....	30
3. Results.....	37
4. Discussion.....	41
<b>IV. Quantitative MRI measurements in Neuromyelitis Optica</b>	
1. Introduction.....	45
2. Case report and Methods.....	45
3. Results.....	48
4. Discussion.....	51
<b>V. PEER-REVIEWED PUBLICATIONS OF THE AUTHOR</b> .....	53
<b>VI. References</b> .....	57

## **Acknowledgments:**

The work presented here in this thesis could not have been carried out without the enormous help of the neuroclinical research group of Pécs.

First, I would like to thank my chief supervisor Attila Schwarcz, and my co-supervisors József Janszky and Tamás Dóczi for providing me the opportunity and scientific background for my work. They helped me all along from the very beginning and set the path of my interest. At the same place I would like to thank the Diagnostic Center of Pécs especially Béla Németh for providing the financial and material background of my work, and also Ferenc Kövér, Péter Bogner, Zoltán Pfund, Zsolt Illés and Sámuel Komoly, those who oriented me more to the applied clinical practice. Special thanks must be paid to Gergely Orsi, Gábor Perlaki, Csaba Szalay and Roy Steier for working together as a team and also as friends.

Furthermore, I would like to thank Tibor Auer and Zoltán Berente who helped me by the beginning, by teaching me the basics. Last but not at least I am thankful to the whole staff of the PDK, the department of Neurosurgery including the neurobiological lab and Physiology of the University of Pécs.

## **Abbreviations:**

**ADC:** Apparent diffusion coefficient.

**Cho:** Choline.

**Cr:** Creatine.

**CV:** Coefficient of variation.

**DWI:** Diffusion weighted imaging.

**SWI:** Susceptibility weighted imaging

**PWI:** Perfusion weighted imaging

**FLAIR:** Fluid attenuated inversion recovery

**EPI:** Echo planar imaging.

**MRI:** Magnetic resonance imaging.

**MRS:** Magnetic resonance spectroscopy.

**mT/m:** Militesla/meter.

**NAA:** N-acethyl-aspartate.

**PRESS:** point resolved spectroscopy sequence.

**RF:** Radio frequency

**ROI:** Region of interest.

**Spin:** impulse moment of the particles (practically magnetic moment)

**T1-T2w** - T1-T2 weighted imaging

**SNR:** Signal to noise ratio.

## **I. Introduction**

### **I.1. Preface**

Clinical magnetic resonance imaging in practice is dominated by qualitative imaging that is based on the contrast differences of certain magnetic relaxation and other physical properties of the tissues. Qualitative imaging gives a cross-sectional information of the imaged phenomena (eg. T1-T2 relaxation, diffusion etc.) but it cannot identify the exact background. It is suitable for tissue differentiation only when there is enough contrast between two different samples, and gives only a coarse and relative information for comparison. Quantitative imaging steps further, by identifying the background of the measured phenomena in the way of acquiring and analyzing a series of qualitative images, thus allowing more precise characterization and follow up. In clinical practice the quantitative approach is not generally utilized however research and scientific MR experiments are mainly based on quantitative measurements. The main reason for the clinical underrepresentation is that quantitative approach is time consuming and demands special knowledge for the measurements, however nowadays with state of the art scanners and software they are slowly starting to be introduced to routine imaging. In Hungary there are only a few MR research sites, and only a part of them are dealing with quantitative MRI. During my PhD training my aim was to acquire feasible quantitative imaging methods (T1-T2 relaxation, bi-exponential water diffusion, perfusion, quantitative spectroscopy) through scientific experiments, and implement the knowledge both in the research and clinical practice.

## I.2 Basics of NMR-MRI

The NMR phenomenon describes how atomic particles react to electromagnetic energy within external magnetic fields. It was independently described by Bloch and Purcell in 1946 both were awarded the Nobel prize in 1952.

Particles building up the atoms due to their inner structure and constant movement generate an own small magnetic field. This magnetic feature (spin) interact with external magnetic fields in a way determined by such strict energetic rules. Basically two different energetic states can be observed for a certain particle placed within an external magnetic field according to how they precess along the orientation of the external field. A lower energy: to align it's own small magnetic field parallel, and a higher energy: to align it anti-parallel(opposite direction) state is present. Utilizing the energetic difference of these two states is the basis of NMR: we excite the particles from the lower energy state to the higher one (flipping them from parallel to the anti-parallel orientation) and after the excitation we observe their relaxation back to the lower energetic state (how they flip back to parallel). Despite the minute size of these particles their movement as magnets during the relaxation induces enough current in our finely tuned antennas to measure. This signal is used to reconstruct every MR image, spectra, etc.

The excited particles need time to go back to the lower energy state to be able to be excited again. The time describing this re-excitability is called T1 time and T1 time means the time (in ms) to take for ~63% of an excited particle population to fully relax (to be able to re-excited again). At the relaxed state particles are aligned according to the thermal equilibrium, and they from a lattice structure, so returning to this structure is called spin-lattice relaxation (T1).

If we observe the signal induced in our antennas during relaxation we will notice an exponential signal decay. In a homogenous magnetic field the signal will decay exponentially and the time

describing the decay is called the T2 time. The T2 time means (in ms) the time for the maximal signal measured right after excitation to decay by ~63%. The current induced in the antenna is mostly affected by the spin-spin coherence and interaction hence the name spin-spin relaxation. In a non-homogenous magnetic field the decay is accelerated and called T2\* relaxation. If we want to observe pure T2 decay we have to apply special pulses (eg. 180° refocusing pulse in spin-echo) to compensate the spin dephasing effect of field inhomogeneity.

However all particles (proton, neutron, electron) have some degree of magnetic feature due to their inner structure, protons have several order higher in magnitude, that enables them to be the most "easily" detected and measured. Particles within the nuclei are organized in a very strict energetic way according to magnetic moments(they pair up at different energy levels), due to this we can interact only with the magnetic moment of unpaired particles. Utilizing these two features everyday NMR is based upon unpaired proton measurements of nuclei with odd mass number: H<sup>1</sup>, C<sup>13</sup>, P<sup>31</sup>, etc.

The excitation is performed with an electro magnetic pulse (RF pulse) having the same frequency as the precession of the protons that results in "resonance" a very efficient energy transfer. (Consequently for signal reception our coils are also tuned to this frequency.) At a certain magnetic field strength the resonance frequency of protons are basically influenced by the host nuclei, and in a smaller degree by the surrounding of the chemical environment. The big variety of measurable nuclei in molecules results in wide variety of resonance frequency that is technically impossible to be covered by one machine.

Human scanners are tuned to the resonance frequency of protons(H<sup>1</sup>) in water. Some other molecules close to this resonance frequency range containing protons can also be detected like -CH<sub>2</sub> and -CH<sub>3</sub> chains in fat and some other molecules like choline and creatine etc. To be able to measure other nuclei on a clinical scanner eg. C<sup>13</sup>, P<sup>31</sup> a dedicated so called multinuclear

transmitter-receiver RF coil system is needed. Consequently human scanner MRI is water proton NMR(I). My thesis is focusing on this type of experiments.

### **I.3 The way to MR Imaging**

In the beginning of the 20th century quantum mechanics revolutionized the way of thinking about the behavior of atomic particles. The magnetic moment of the proton was first measured by Estermann and Stern in 1933 and verified in 1938 by Rabi [1-2]. The MRI revolution was initiated in 1946 when the NMR phenomena was presented in practice by two different research groups of Purcell and Bloch in 1946 [3-4]. The discovery of spin-echo generation [5] by Hahn was a major step forward. These days MR measurements were performed only by some dedicated sites on so called "state of the art" analog spectrometers. Later the introduction of digital signal processing [6-7] made the methodology applicable to wider audience. The signal changes of the whole sample were detected with these machines and mostly the main relaxation parameters (T1-T2) were studied. Different tissue relaxation parameters were first confirmed in animal and somewhat later in human [8-9] tissue samples. Meanwhile Lauterbur published the principles of the imaging [10]. In 1977 the first image of the human body was presented [11] and MRI was born and still developing in an enormous rate revolutionizing diagnostic imaging.

### **I.4 Qualitative imaging**

Image interpretation based on intensity differences (contrast) between different tissue qualities is called qualitative imaging. Contrast generation in MRI is one of the main strength of the method compared to any other imaging modality. Almost infinite variations of contrasts can be achieved by combining different excitation and signal detection times with the virtually infinite number of electro-magnetic pulses. The main goal is to choose and adjust the imaging sequence in order to

achieve the final desired MRI contrast. The measured MR signal is always determined by multiple effects (T1-T2 relaxation, diffusion, perfusion, susceptibility, etc.) pure contrast generation is impossible, hence the weighting index always used by the sequence names. The aim is to set up the imaging sequence in a way of emphasizing the desired contrast effect the most and suppressing the others to the lowest possible.

The first imaging sequences were tuned to show the T1 and T2 relaxation differences of the tissues [12-14]. T1-T2w images proved to be so useful that even nowadays they represent the basis of imaging protocols. Somewhat later by applying special motion sensitizing gradients within a sequence [15-16] weighting on water diffusion became possible. Nowadays plenty of contrast weighting techniques are available: T1,T2,T2\*, proton density, FLAIR, DWI, SWI,PWI etc. . The goal is to always choose the sequence most suitable to answer our question.

The pitfall of qualitative imaging is that exact quantification is not possible, and it only shows a cross sectional information of the weighted effect (figure 1) not the exact background, while contrast is very sensitive to technical parameters. However fast imaging time and simple applicability is the main advantage that puts the method in first place in everyday diagnostics.

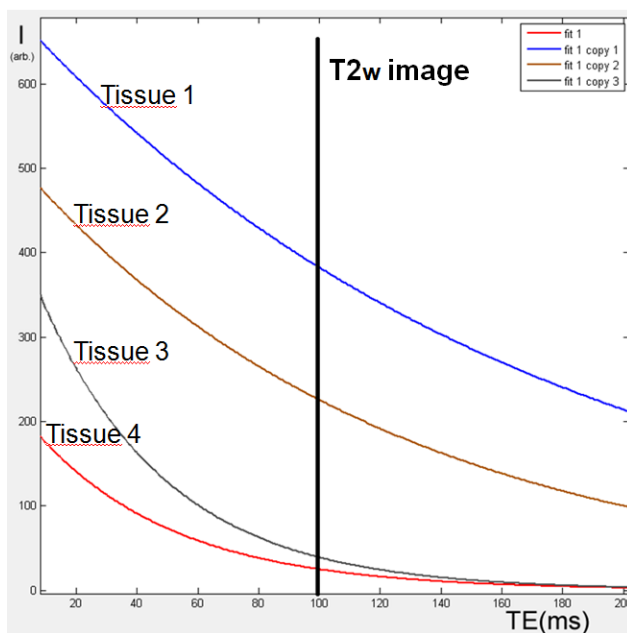


Figure 1. Quantitative vs. Qualitative imaging. This figure shows the T2 relaxation time curves obtained from quantitative measurements of 4 different tissues. The quantitative data describes the signal intensity during the whole T2 relaxation process.

A cross sectional line at TE:100ms represents what a T2w qualitative image capture from the T2 relaxation process. Choosing the optimal weighting parameter (eg. echo time) is crucial in qualitative imaging for obtaining optimal tissue contrast, however the whole relaxation course remains a "black box".

## I.5 Quantitative Imaging

While qualitative imaging gives only a cross-sectional contrast based information, the quantitative approach steps further, and describes the signal courses of the processes in a standardized numerical way (Figure 1.). T1, T2 relaxation, diffusion-perfusion parameters, blood velocity, metabolite concentrations, magnetization transfer and many other parameters can be determined quantitatively by MRI [17-18]. An exact determination of the desired effects allow a more detailed insight and standardized basis of comparison, tissue characterization and follow up. For quantification a more detailed approach is needed. Generally it is performed in a way of analyzing a series of qualitative images, where the time course of the signal change is controlled by the change of an imaging parameter. By fitting the signal change against the parameter change is the regular way how a quantitative parameter is derived (figure 2)

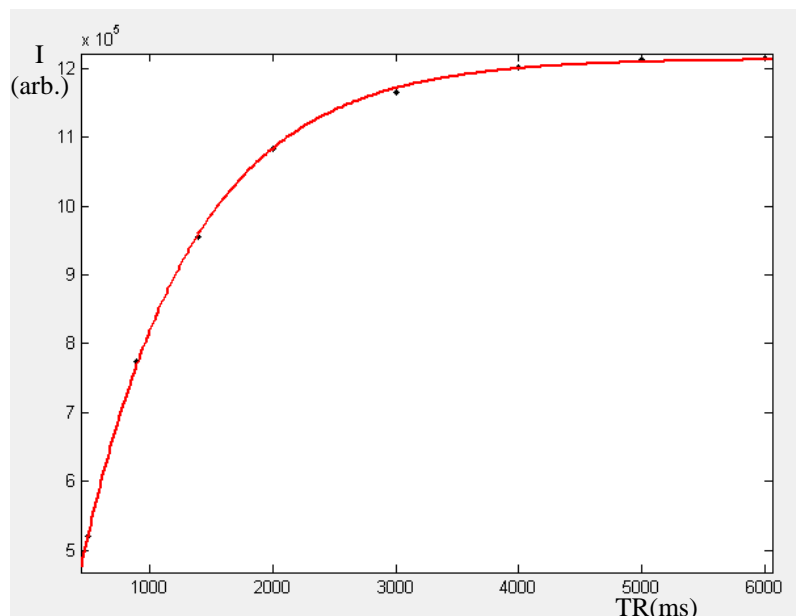


Figure 2: T1 relaxometry is performed in a way of analyzing a series of T1w qualitative images differing only in the repetition time. The measured MR signal of a sample is presented by different repetition times. By fitting a curve on the intensities a quantitative parameter of T1 time can be calculated.

## II. Quantitative proton MRI and MRS of the rat brain with a 3 T clinical MR scanner

### II.1 Introduction

Magnetic resonance imaging (MRI) in animals has the substantial advantage that the evolution of a modeled pathology can be followed *in vivo*. The complicated signal changes detected in human pathologies (e.g., multiexponential diffusion) can be modeled and the background of these signal changes may be elucidated via the morphology [19]. However, the dedicated small-animal (i.e., rat and mouse) scanners with strong gradient coils can be quite expensive. Many clinically-based researchers, and especially radiologists, do not have access to such MR apparatus. To circumvent this situation much effort has been devoted proving that large-bore clinical MR scanners have the ability to perform small-animal imaging with acceptable quality [20—35]. Most of the reported successful rat MRI measurements performed with human scanners provided merely qualitative data: only  $T1$  or  $T2$ -weighted images were produced [27] together with quantitative  $ADC$  data [24,36]. The reason for refraining from quantitative MRI is that the low signal to noise ratio (SNR) and inappropriate MR sequences may yield very inaccurate results. This is also obvious in the case of dedicated small-animal scanners operating at higher magnetic field strength, e.g., the reported  $T1$  values for the rat brain range from 928 ms to 1690 ms at 4.7 T in the literature [37,38]. This situation demonstrates the merit of a recently published paper in which  $T1$   $T2$  and magnetization transfer were determined *in vitro* with high accuracy in different tissue types at 3T [39]. These latter authors state that the literature regarding  $T1$  and  $T2$  data at 3 T is surprisingly limited. Quantitative MRI would be important, for instance, in brain edema studies in which the extent of the edema appears identical (i.e., the same hypo- or hyperintense area is seen on the images) but  $T1$  and  $T2$  may be significantly

different among animals depending on the water content [40,41]. As regards the spectroscopy of small animals on human scanners, only a few papers are available in the literature [42,43].

Combination of the relatively high SNR of a 3 T human scanner with a strong insert gradient coil make DTI feasible in the rat brain [44]. It was demonstrated that a field strength of 3 T allows not only better human imaging, but also small-animal imaging with a spatial resolution comparable to those obtained with dedicated small-bore magnets [27,30,45]. Accordingly, 3 T clinical scanners may readily be employed in small-animal imaging, and expensive small-bore systems are not necessary for most applications. The advantage of a clinical MRI scanner is that it has very homogenous B1 field; however, the smaller gradient amplitude and the lack of flexibility in pulse sequences imposes problems to overcome. The aim of our study was to demonstrate the capability of a 3 T human scanner in performing quantitative imaging in small-animals. The study was carried out using commercial coils and commercial MR sequences; no sequence manipulation or extra MR hardware was applied.

## **II. 2. Materials and Methods:**

### **Phantom experiments**

A group of solutions was prepared with increasing gadolinium (Magnevist, Bayer®) concentrations. The solutions were measured by three independent imaging methods in order to test the accuracy of the measurement of  $T1$ : (i) saturation recovery spin echo imaging single slice, (ii) inversion recovery spin echo imaging single slice and (iii) multislice inversion recovery turbo spin echo imaging. Method (iii) was then used in an animal study (see below). The same coil setup was used for phantom and animal experiments (i.e., no major difference in filling factor).

### **Animals**

The experiments were carried out on eight Wistar rats (250—300 g, three females, five males). The rats were intubated and anesthetized with 1.5% isoflurane in a 70/30 mixture of N<sub>2</sub>O and O<sub>2</sub>. The rectal temperature of the animals was maintained between 36.5 and 37.5 °C throughout the experiments by using an isothermal pad (Deltaphase®, Braintree Scientific Inc., Braintree, USA). The head of each rat was fixed in a custom-built plastic head holder and placed through a loop RF coil (Fig. 3). After MRI and MRS examinations, the animals were sacrificed with an overdose of isoflurane. The brains were rapidly removed in a humid chamber, brains weighed immediately and dried to constant weight at 90 °C. The percentage water content ( $W$ ) of each sample was calculated according to Eq. (1):

$W = 100 \times (\text{wet weight} - \text{dry weight}) / \text{wet weight} (1)$

was utilized in the quantitative MRS calibration.

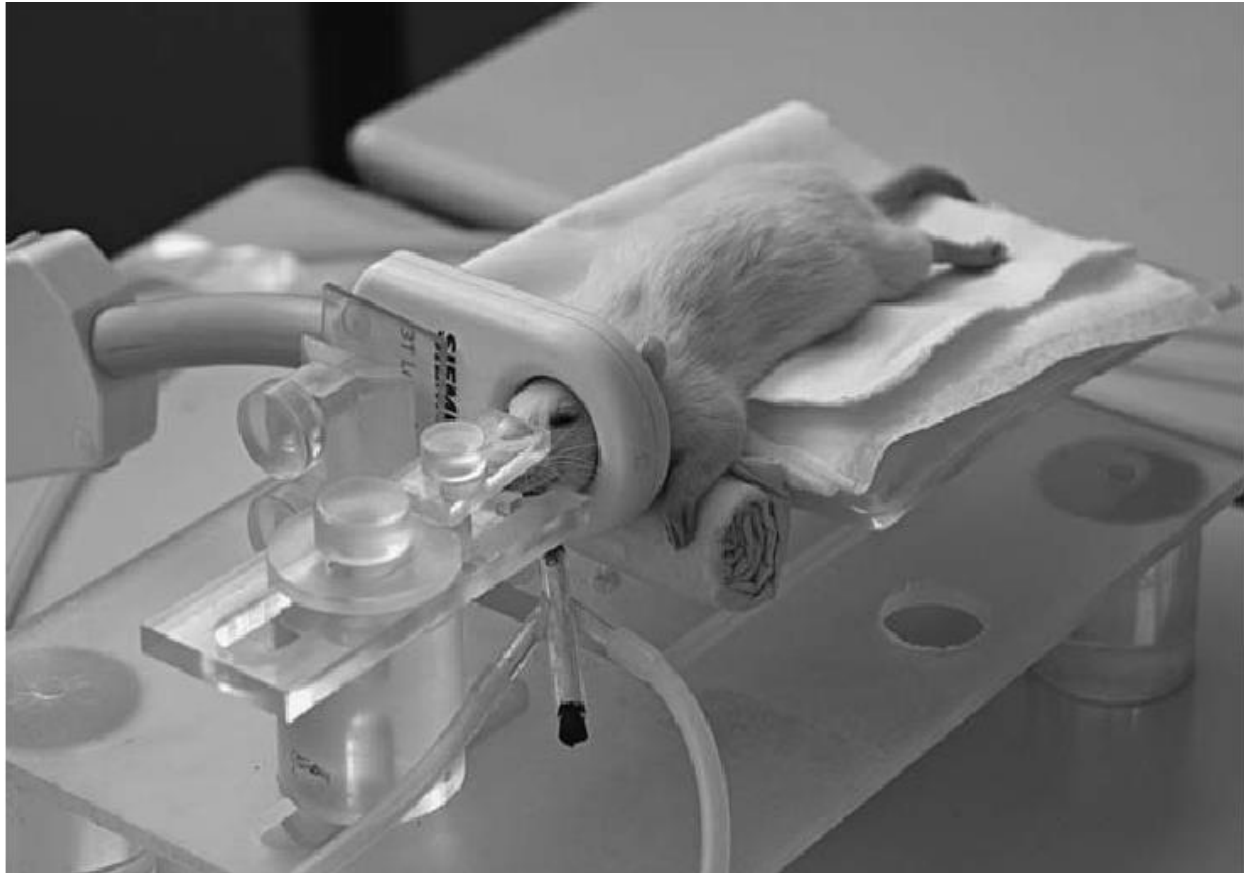


*Figure 3: The custom-built head holder with the 40mm (i.d.) loop coil. The rat is intubated and anesthetized.*

## **MRI and MRS**

MRI was performed on a 3.0 T clinical MRI scanner (Magnetom TIM Trio, Siemens Medical Solutions, Erlangen, Germany) with a field gradient strength of 40 mT/m. Excitation was performed with the body coil, while a commercial loop RF coil with an inner diameter of 40mm (Siemens Medical Solutions, Erlangen, Germany) was applied for signal detection. After the acquisition of scout images of the rat brain,  $T_1$ ,  $T_2$ , and diffusion measurements were

performed. The MRI protocol was followed by MRS experiments. High-resolution  $T_2$ -weighted MRI was also performed in three rats in separate experiments carried out by a turbo spin echo imaging sequence:

$TR/TE = 3000/76$  ms, slice thickness = 0.13mm,  $FOV = 33 \times 33 \text{mm}^2$ ,  $256 \times 256$  pixel matrix, bandwidth = 40 Hz/pixel, fat suppression with spectral attenuated inversion recovery method (SPAIR), number of acquisitions = 1.

$T_1$  was determined by an inversion recovery method, applying a turbo spin echo imaging sequence: slice selective inversion pulse,  $TR/TE = 4200/15$  ms, slice thickness=1mm, distance factor=0mm with two concatenations (i.e., no gap, two interleaved series of slices),  $FOV=31 \times 31 \text{mm}^2$ ,  $128 \times 128$  pixel matrix, bandwidth = 300 Hz/pixel, number of acquisitions = 1, echo train length = 8, number of slices = 20, inversion times = 300, 700, 1300, 1900, 2400 and 2800 ms.

$T_2$  was determined by the standard spin echo imaging version of the CPMG sequence:  $TR/TE = 2600/12.1, 24.2, 36.3, 48.4, 60.5, 72.6, 84.7, 96.8, 108.9$  and 121 ms, slice-thickness = 1mm, distance factor=0mm (i.e., no gap),  $FOV=33 \times 33 \text{mm}^2$ ,  $128 \times 128$  pixel matrix, bandwidth = 175 Hz/pixel, number of acquisitions = 1, number of slices = 20.

Diffusion was determined with a trace-weighted singleshot echo planar imaging sequence:  $TR/TE = 4000/119$  ms, slice thickness = 1.9mm, distance factor=0mm (i.e., no gap),  $FOV=30 \times 95 \text{mm}^2$ ,  $40 \times 128$  pixel matrix, bandwidth = 830 Hz/pixel, number of acquisitions = 4, number of slices = 14,  $b$  values: 0, 500, 1000, 2000, 3000, 4000, 5000 and 6000  $\text{s}/\text{mm}^2$ .

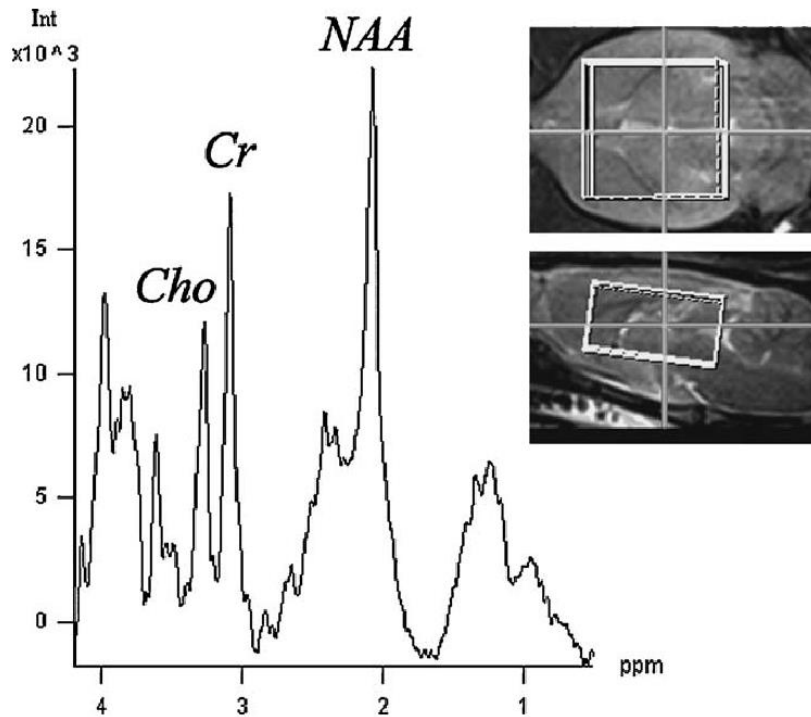


**Figure 4.:** This figure shows the position of the  $5 \times 10 \times 10 \text{ mm}$  voxel in the rat brain used for spectroscopy (a) and also the corresponding proton spectrum (b). The major peaks are labeled (NAA: N-acetyl-aspartate; Cho: choline; Cr: total creatine).

Before MRS acquisition, a  $10 \times 10 \times 5 \text{ mm}$  voxel was defined in the middle of the rat brain (Fig. 4). After localized manual shimming and water suppression adjustment, fully relaxed short-echo-time proton MR spectra (PRESS,  $TR/TE = 6000/30 \text{ ms}$ , 64 accumulations) were acquired. Water suppression was accomplished with a chemical shiftselective sequence [CHESS] pulse. At the end of the MRS experiment, a reference water signal for the calibration of metabolite concentration was also acquired by turning off the water suppression. The total experimental protocol lasted for  $\sim 36 \text{ min}$  comprising (i) 13 min for  $T1$  measurement, (ii) 4 min for  $T2$  measurement, (iii) 6 min for  $ADC$  quantification, (iv) 13 min for quantitative proton spectroscopy including manual adjustments. The acquisition time for high-resolution  $T2$ -weighted imaging was 146 min.

## Data processing

*TI* maps were calculated pixelwise from the images with different inversion times applying either a standard twoparameter fit (Eq. (2) [46]) or a three-parameter fit that accounts for RF pulse imperfections (Eq. (3) [47,48]).

$$M = |M0 * (1 - 2 * \exp(-TI/T1) + \exp(-TR/T1))| \quad (2)$$

where *M* is the measured signal intensity, *M0* is the signal intensity at thermal equilibrium, *TI* is the inversion time, and *TR* is the repetition time.

$$M = |A + B * \exp(-TI/T1)| \quad (3)$$

where *A* and *B* are constants incorporating *M0* and corrections for imperfect RF pulses (i.e., deviation from the nominal flip angle).

*T2* maps were produced from the pixelwise fit of Eq. (4), assuming monoexponential signal decay:

$$M = M0 * \exp(-TE/T2) \quad (4)$$

*ADC* maps were also generated by a monoexponential fit of signal intensities in the low *b* value range (i.e., *b*value = 0, 500 and 1000 s/mm<sup>2</sup>). A manual coregistration of *ADC* maps with *TI* maps was performed in each slice (i.e., two-dimensional stretching) in order to decrease the EPI distortion artifacts. The *ADC* values of the rat cortex were broken down into *ADC<sub>fast</sub>* and *ADC<sub>slow</sub>* by applying a biexponential fit throughout the whole *b* value range (Eq. (5)).

$$M/M0 = f_{fast} \exp(-b * ADC_{fast}) + f_{slow} \exp(-b * ADC_{slow}) \quad (5)$$

where *M* is the signal in the presence of diffusion sensitization, *M0* is that in the absence of

diffusion sensitization,  $ADC_{fast}$  and  $ADC_{slow}$  are apparent diffusion coefficient values, and  $f_{fast}$  and  $f_{slow}$  are the contributions to the signal of the fast and slow-diffusing water compartments.

Freehand regions of interests (ROIs) were drawn on  $T1$ ,  $T2$  and  $ADC$  maps to yield mean values (Fig. 5). Raw spectroscopic data were postprocessed by using a Siemens Leonardo Workstation with built-in Siemens spectroscopy software. We applied a Hanning filter and zero filling to 2048 data points before Fourier transformation. After manual baseline and phase correction, an automatic fit was applied to the Fourier-transformed spectra, and the peak integrals of water, choline (Cho), creatine (Cr) and N-acetyl-aspartate (NAA) were determined. The molar tissue water content ( $MWC$ ) was calculated from the tissue water content ( $W$ ) determined by the wet/dry method and the molar concentration of pure water (55.6 mol/L). Finally, the absolute metabolite tissue concentrations

were calculated from:

$$C = IM * MWC * 2 / (n * IW) \quad (6)$$

where  $C$  is the molar concentration of the metabolite,  $n$  is the number of resonating protons,  $IM$  is the peak integral of a given metabolite, and  $IW$  is the peak integral of water. This formula only applies for spectra with long TR and short TE.

### **Statistical analysis**

In phantom experiments only one ROI was used for each solution, standard deviation represents the variability of  $T1$  within the ROI. Concerning the animal study, two ROIs were placed in the cortex on both sides of the brain (Fig. 6). Within one animal, mean value and standard deviation was calculated by taking into account pixelwise data of both ROIs. The Coefficient of Variation

(CV) was calculated (i.e., ratio of the SD to the mean) to normalize the SD in animal experiments.

## **II.3 Results**

### **Phantom experiments**

All three methods, (i) saturation recovery spin echo imaging single slice, (ii) inversion recovery spin echo imaging single slice and (iii) multislice inversion recovery turbo spin echo imaging, yielded similar  $T1$  values with low standard deviation (Table 1). Both the two- and three-parameter fit gave accurate results in multislice inversion recovery turbo spin echo imaging (Table 1). Multislice inversion recovery turbo spin echo sequence was chosen for in vivo measurements because it provided a multislice acquisition in a reasonable time frame.

### **High-resolution MRI**

Although the focus of our study was quantitative MRI and MRS, the high-resolution  $T2$  weighted image shows the capabilities of a 3 T human scanner (Fig. 5). A microscopic resolution of  $130 \times 130 \times 130 \mu\text{m}^3$  was achieved (Signal-to noise ratio = 30).



**Figure 5.**

High-resolution ( $130 \times 130 \times 130 \mu\text{m}^3$ ) T2-weighted image of the rat brain (turbo spin echo:  $TR/TE$  3000 ms/76 ms).

### T1 and T2 in the rat brain

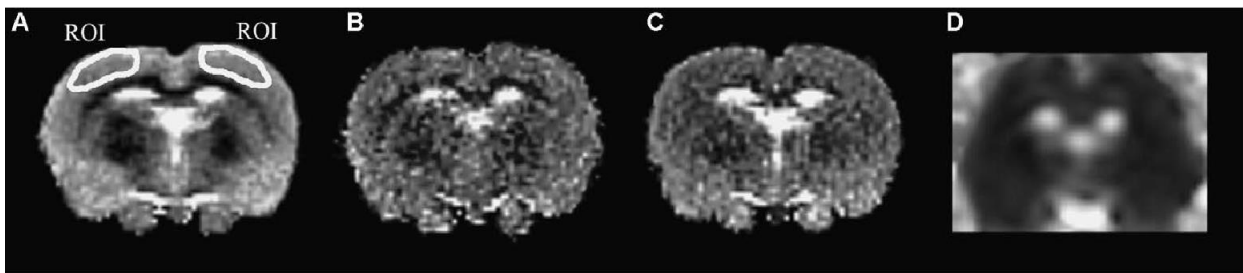


**Figure 6.** *T1 maps of the rat brain generated by two- (a) or three- (b) parameter fit of the turbo spin echo inversion recovery data. The T1 map generated by the two-parameter fit demonstrates more homogeneity in the cortex, and accordingly a lower SD (see Table 2). The regions of interest (ROI) used for the cortex are shown (a). T2 (c) and ADC (d) maps of the same slice are also presented.*

T1 maps (Fig. 6) were generated by applying either the two-parameter fit or the three-parameter fit. The two parameter fit gave a mean  $T1$  value of  $961 \pm 2.5\%$  ms for the cortex while the three-parameter fit gave significantly ( $p < 4.3 \times 10^{-7}$ , paired  $t$ -test) larger  $T1$  value of  $1272 \pm 6.7\%$  ms (Table 2). The CV of  $T1$  was less in the two parameter fit (Table 2). Fig. 7. demonstrates the difference between two- and the three-parameter fit in the in vivo data obtained from the cortex as free hand ROI. It is clear that the two-parameter fit is not a good model ( $r^2 = 0.96$ ), while the

three-parameter fit gives a nearly perfect match ( $r^2 = 0.99$ ) (Fig. 7). However, due to the larger CV, the three-parameter fit resulted in less smooth  $T1$  maps than those produced via the two-parameter fit (Fig. 6). The  $T2$  maps (Fig. 6) produced a mean  $T2$  value of  $75 \pm 2\%$  ms for the rat cortex. The standard deviation was less than that in the  $T1$  measurement (Table 2).

Gadolinium cc.	Spinecho Saturation Recovery single slice	Spinecho Inversion Recovery single slice	Turbospinecho Inversion Recovery multislice	
			<i>Fit1</i>	<i>Fit2</i>
0.266	915 ± 2	899 ± 3	909 ± 11	933 ± 15
0.2	1184 ± 3	1133 ± 13	1078 ± 32	1068 ± 26
0.133	1440 ± 2	1335 ± 18	1360 ± 19	1405 ± 19
0.083	1865 ± 5	1815 ± 28	1726 ± 11	1764 ± 67
0.053	2038 ± 10	2145 ± 45	1997 ± 21	2129 ± 43

**Table 1.**

$T_1$  values (ms) obtained for gadolinium solutions (mmol/l). Turbospinecho inversion recovery data were fitted using either two (Fit1) or three parameter fit (Fit2). The equations for fit are presented in the methods section.

	$T_1$	$T_2$	$ADC_{mono}$	$ADC_{fast}$	$ADC_{slow}$	$p_{fast}$	$p_{slow}$	
	<i>Fit1</i>	<i>Fit2</i>						
mean	961	1272	75	6.02	9.36	2.04	74.3	25.7
CV(%)	2,5	6,7	2	3,8	9,7	16	6,1	17,5

**Table 2.** Quantitative MR parameters measured in the rat brain.  $T_1$  data were fitted using either two (Fit1) or three parameter fit (Fit2). The equations for the fits are presented in the methods section. Means and coefficients of variations(CV) are presented

$T_1$  and  $T_2$  times are shown in milliseconds,  $ADC_{mono}$ ,  $ADC_{fast}$ ,  $ADC_{slow}$  in ( $\times 10^{-4} \text{mm}^2 \text{s}^{-1}$ )

$p_{fast}$  and  $p_{slow}$  in (%)

## Diffusion

The *ADC* maps (Fig. 6) were produced by using only the low *b* value range (i.e., 0, 500 and 1000 s/mm<sup>2</sup>). The spatial resolution of *ADC* maps is much lower than that of *T1* and *T2* maps with obvious image blurring. The low image quality is mainly due to the gradient limitations of the scanner and not to the low SNR. The quantitative *ADC* data are presented in Table 2. The large voxel size in DWI produced a high SNR which allowed the acquisition of diffusion images with larger *b* values. The SNR was > 15 even on the images with *b*=6000 s/mm<sup>2</sup>. Via the biexponential approach throughout the whole *b* value range *ADC<sub>fast</sub>* and *ADC<sub>slow</sub>* with the corresponding volume fractions were determined with acceptable standard deviation.

## Spectroscopy

	Cho	Cr	NAA
mean	1,77	6,25	8,78
CV(%)	21	25	14

**Table 3.** Metabolite concentrations (mmol/l) of the rat brain measured by proton spectroscopy.

Means and coefficients of variations (CV) are presented.

The localized manual shimming to the voxel was essential in the signal acquisition. A representative spectrum of the rat brain is shown in Fig. 4. The SNR for the NAA peak was ~17 which could permit a smaller voxel size, but reduction of the voxel size was not possible because of limitations in the commercial PRESS sequence. The mean water concentration (*W*) in

the rat brain was  $78.0 \pm 0.5\%$ . It was used for calibration of the water peak in Eq. (6). The metabolite concentrations determined for NAA, Cr and Cho are presented in Table 3.

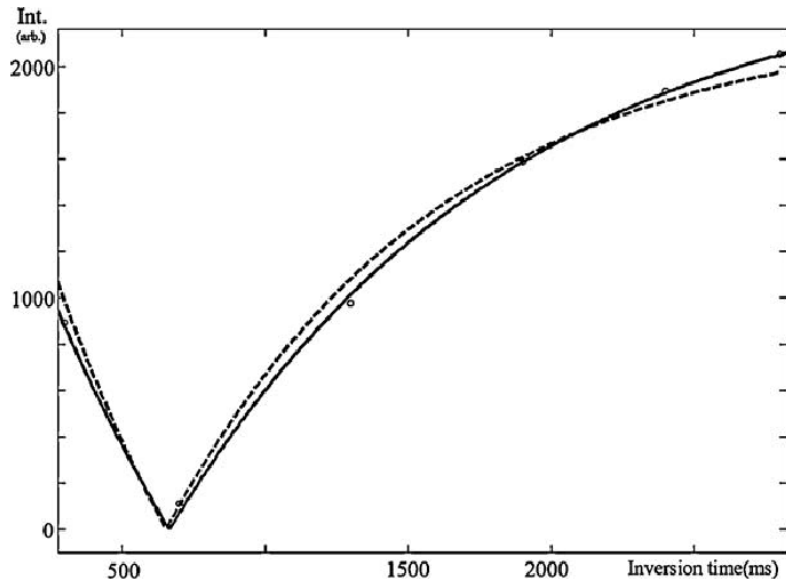


**Figure 7: Comparison of two- and three- parameter fits used for  $T1$  measurement.** The equations for the fits are presented in the Methods section. The intensity (arbitrary units) obtained from a rat cortex is plotted against the inversion time (ms). Dashed and continuous lines correspond to the two- and threeparameter fits, respectively.

## Discussion

The advances in the technology of clinical MR scanners permit high-quality small-animal imaging [20,30,44,45]. MR spectroscopy has also become possible in small animals in consequence of the higher magnetic field strength and custom-made coils [42,43]. It was recently demonstrated that mouse brain MRI is feasible with microscopic resolution even at the relatively low magnetic field of 2.35 T [49]. Although this was not the focus of our study, we succeeded in performing rat brain MRI with microscopic resolution. Long measurement time is usual in MRI anatomical studies of small animals [45,49]. Quantitative MRI and MRS data acquired with clinical scanners are seldom reported [50,51], though they would be important in the follow-up of in vivo pathologies. For instance,  $T1$  values of the brain may be converted to

water content, so that brain edema can be measured in vivo [41,52—54]. However, the pitfall of in vivo  $T1$  measurements is clearly demonstrated by comparing the in vivo and in vitro data in the present study. Both two- and the three- parameter fits gave accurate  $T1$  values for the gadolinium solutions; however, the two-parameter fit underestimates  $T1$  in vivo. Fig. 8 shows the dependence of the published  $T1$  values for the rat cortex [37,38,51,53,55—69] on the magnetic field strength. Only empirical data are available for  $T1$  of brain tissue vs magnetic field [30]. A  $T1$  value of ~1270 ms for 3 T is estimated by fitting either a general equation of Rooney et al. [30] or a simple linear trendline (Fig. 8). When this predicted  $T1$  is taken into account, only the three-parameter fit furnishes accurate  $T1$  values. Failure of the two-parameter fit in vivo is probably explained by the RF imperfections which results in incomplete inversion and refocusing. It should also be noted that the CV is larger when the three-parameter fit is used than that produced by the two-parameter fit. Nevertheless, this ~7% CV obtained with a clinical scanner is still within the CV range observed for small-bore systems: 2—10% [58,60,61,70]. Further, on the basis of a meta-analysis of the human  $T1$  at 1.5 T, Tofts and Boulay [71] speculated that biological variation of  $T1$  in the brain should be around 5%. Fig. 9 shows the literature  $T2$  values for the rat brain as a function of magnetic field strength [37,38,57—59,63,65—68].  $T2$  data are often reported because of the direct relationship with brain edema [40] and also because of the simple and rapid measuring method. Similarly to  $T1$  the  $T2$  data also suggest a linear dependency on magnetic field strength (Fig. 8). This linear relationship indicates that  $T2$  for the rat brain should be ~76 ms at 3 T which is in very good agreement with our data. The CV of  $T2$  is smaller (~2%) than that of  $T1$ , probably as a result of the lower sensitivity of measurement in RF field problems.

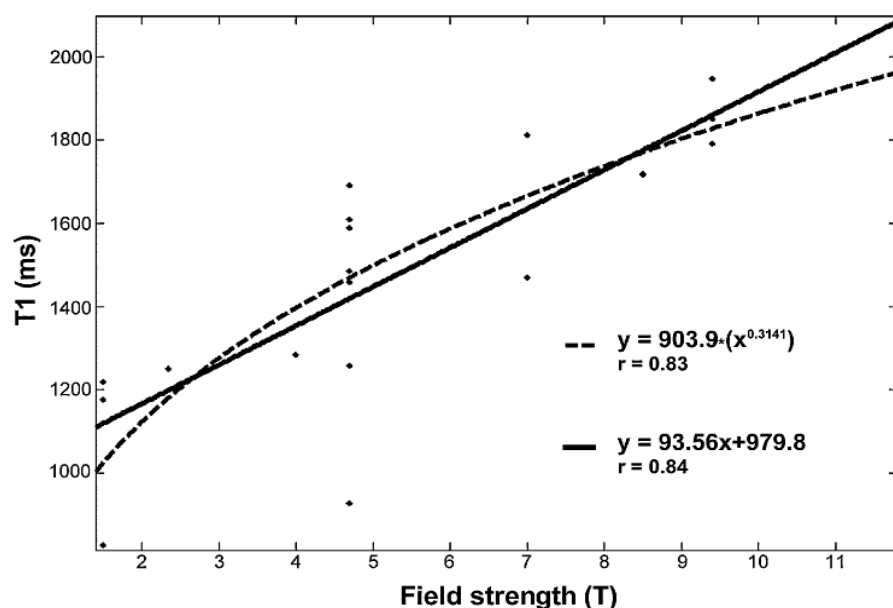


**Figure 8.:** This figure shows the dependence of the published T1 values for the rat brain [37,38,51,53,55—68] on the magnetic field strength. There is a clear linear trend (continuous line) between T1 and the magnetic field strength in the range of 1.5—11.4 T. The figure also shows the empirical relationship (dashed line) between T1 and magnetic field strength derived from [69].

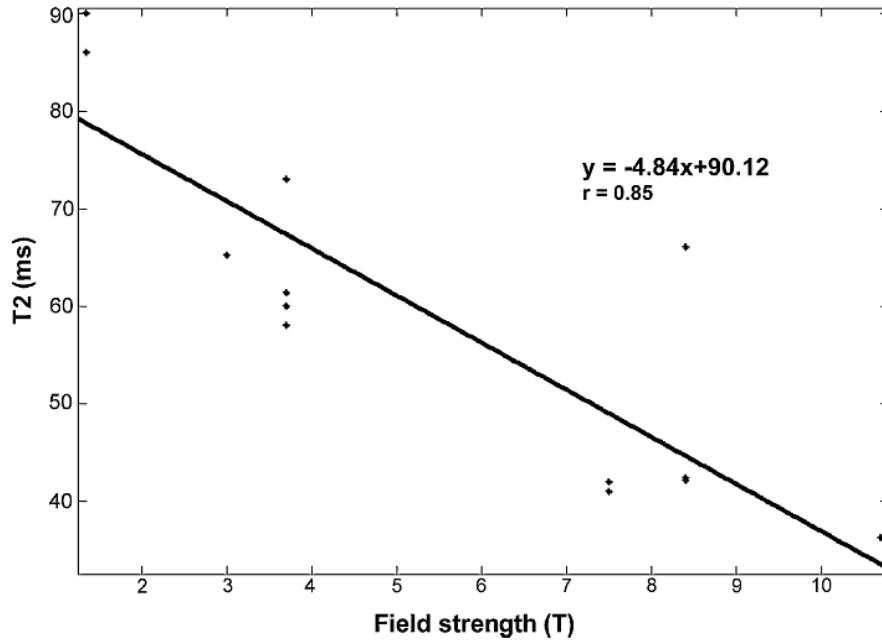


**Figure 9.:** This figure shows the dependence of the published T2 values for the rat brain [19,37,39,43,49,53,72—74,76] on the magnetic field strength. There is a clear linear trend between T2 and the magnetic field strength.

Quantitative, low  $b$  value range ADC data were earlier obtained on human scanners, mostly in stroke studies of the rat brain [24,36]. Although a good SNR can be achieved with the current set-up at 3 T, the limitations (mainly in gradients) did not allow better spatial resolution with the applied EPI sequence. Similar ADC images with low spatial resolution obtained with clinical scanners have been reported in the literature at 3 T [30]. The high SNR originating from the low spatial resolution allows larger  $b$  values. The biexponential analysis of the diffusion data yielded  $ADC_{fast}$  and  $ADC_{slow}$  values in very good agreement with those to be found in the literature [19,72,73].  $ADC_{mono}$ , ( $\times 10^{-4} \text{ mm}^2\text{s}^{-1}$ ),  $ADC_{slow}$  ( $\times 10^{-4} \text{ mm}^2\text{s}^{-1}$ ) and the volume fractions (%) for instance are almost identical to the results measured in a mouse study [73] at 9.4 T

( $ADC_{mono}$ :  $6.02 \pm 3.8\%$  vs.  $5.90 \pm 3.4\%$ ;  $ADC_{slow}$ :  $2.04 \pm 16.0\%$  vs.  $2.02 \pm 9.9\%$ ;  $p_{fast}$ :  $74 \pm 4.0\%$  vs.  $75 \pm 4.0\%$ ). It is intriguing that despite the markedly increased diffusion and echo time, the volume fractions do not change. Although there is a debate in the literature on the origin of the biexponential signal decay in diffusion measurements, our results clearly demonstrate a good reproducibility regardless of the field strength and echo time. Besides the quantitative imaging experiments, we succeeded in performing quantitative proton MRS in the rat brain. The limitations in the Siemens spectroscopy sequence did not allow the smaller voxel size that could have been achieved according to the SNR of the metabolite spectra. The feasibility of MRS in the rat brain at a 3 T clinical scanner has already been demonstrated through the utilization of special, non-commercial hardware elements [42,43]. Although absolute quantification (i.e., in mmol/l) was not performed, metabolite concentrations were presented in institutional units, normalized to an arbitrary NAA value of 10.0 [62,63]. The metabolite concentrations obtained in our study are in overall agreement with earlier literature results [74,75]. Obviously, the postprocessing steps applied, (mostly baseline correction) and the quantification method (i.e., an external or an internal reference, the principle of reciprocity, etc.) might have a considerable impact on the absolute metabolite concentrations. Nevertheless, our metabolite concentrations and standard deviations almost perfectly match the values reported for the mouse brain using the same water reference strategy [76].

## **Conclusion**

Quantitative  $T1$ ,  $T2$ ,  $ADC$  (including a biexponential approach) and MRS data were obtained at 3 T on a human scanner. The measured  $T1$ ,  $T2$ ,  $ADC$  data appear to be accurate and precise and also comparable to those obtained with dedicated small-bore systems operating at higher magnetic field strength. A microscopic resolution was achieved in the rat brain as concerns

structural imaging. Our results suggest that reliable small animal quantitative NMR measurements can be carried out on new-era high-field clinical scanners. The experiments do not require special MR hardware or software elements. However, the limitations of a clinical scanner in gradient strength and software flexibility should be always taken into account. The results will hopefully encourage others to carry out state-of-the-art rat MRI or MRS on clinical scanners.

### **III. Quantitative MRI Studies of Chronic Brain White Matter Hyperintensities in Migraine Patients**

#### **III. 1 Introduction**

Migraine is a primary headache disorder characterized by recurrent headache attacks associated with temporary symptoms of autonomic nervous system dysfunction, and the attacks can be accompanied by transient focal aura symptoms [77]. Based on magnetic resonance imaging (MRI) findings, migraine is an independent risk factor for supratentorial deep white matter lesions, silent anterior and posterior circulation territory infarcts, and infratentorial hyperintense lesions [78-82]. The brain white matter lesions are more prevalent in migraine patients than in the general population [73], and their presence does not correlate with age [74,75]. The underlying pathogenesis of lesion formation is not completely known, and histopathological analysis of these tissue abnormalities was not performed. Both the disease duration and the attack frequency have an essential role in the lesion evolution, but the effects of comorbid diseases may also contribute to the development of white matter lesions[86,87]. Several attack-related pathophysiological mechanisms have been proposed in the development of lesions[86,87]. Among these factors, the cumulative effect of repeated intracerebral hemodynamic changes, including oligemia and focal hypoperfusion with ischemia/hypoxia below the ischemic threshold have been supposed [80,88].

Even though the repeated migraine attacks affect different parts of the brain, there are regional differences and predilection sites for tissue damage [86,89,90]. The lesions are best visualized on T2-weighted and fluid-attenuated inversion recovery (FLAIR) MRI images as

multiple, ovoid, or circular signal hyperintensities with distinctive borders above (deep and periventricular white matter) and below (brainstem, cerebellum) the tentorium [78,91] (Fig. 10). In the last 2 decades, there have been rapid developments in neuroimaging techniques with a good correlation between the pathology and the MRI findings [92,93]. The nonconventional MRI studies can help in the differentiation of chronic white matter lesions of vascular and nonvascular origin. Usually, these measurements show tissue damage with axonal loss, glial hypocellularity, and decreased cerebral blood flow in both the chronic ischemic and the demyelinating lesions, but in the latter case, signs of demyelination, remyelination, and astrogliosis are also seen [94,95]. Because the advanced MRI methods provide an opportunity to investigate the underlying pathological basis of migraine-related white matter hyperintensities (WMHs), we aimed to measure a variety of different tissue parameters by gaining quantitative MRI data (ie, diffusion and perfusion imaging, T1 and T2 relaxation times, and brain metabolite concentrations) from supratentorial WMHs in interictal states.

Our aims were: (1) to assess the radiological features of WMHs in migraine patients, and (2) to decide whether the measured parameters can support the supposed vascular hypothesis in the development of WMHs. To obtain accurate data on the nature of WMHs, we have examined a homogeneous patient group in which the duration of migraine disease and the migraine attacks were the only known risk factors for the formation of WMHs.

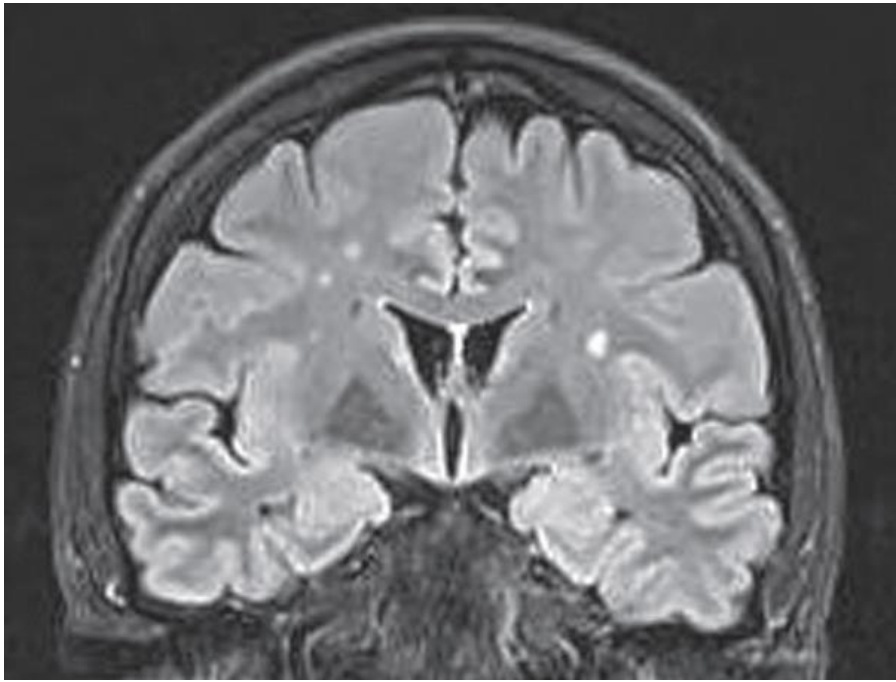


*Fig 10.—A 3.0-Tesla brain magnetic resonance imaging image of a 32-year-old migraine patient without aura. Ovoid highsignal intensities are seen in the white matter of both hemispheres on the coronal fluid-attenuated inversion recovery image. The right side of the image represents the left side of the brain.*

### **III.2 Materials and methods**

**Subjects.**—Seventeen migraine patients (15 females and 2 males, mean age  $\pm$  standard deviation [SD]  $41.1 \pm 11.2$  years, age range 19-65 years) with previously discovered brain WMHs were prospectively enrolled in the study at the Outpatient Headache Department of the Department of Neurology, Medical School, University of Pécs, Hungary. Clinical data of patients are presented in Table 1. All included migraineurs had a 2- to 5-year-long follow-up period before the final MRI studies performed in 2009. The patients were divided into 2 subgroups: 10 patients fulfilled the IHS classification criteria<sup>1</sup> of migraine without aura and 7 patients of migraine with aura. All patients underwent MRI studies 2 or 3 times during the

follow-up period showing FLAIR and T2-weighted WMHs without hypointensity on T1-weighted scans. None of the selected migraine patients had infratentorial signal abnormalities. Further, to gain more accurate information from the WMHs by the MRI scanning protocol, migraineurs were chosen for having at least 1 large supratentorial WMH with normal-appearing white matter (NAWM) area contralaterally. Because the investigated WMHs did not show any changes in size and signal intensity in the follow-up period, these signal abnormalities were at least 2 years old at the time of the final MRI studies. For that reason, the investigated WMHs were defined as chronic WMHs. All MRI studies were performed in a headache-free state, and the patients were not on chronic drug treatments at the time of MRI. All selected patients underwent detailed clinical investigations to exclude the presence of any medical comorbidity that may itself cause WMHs (Table 4). All selected migraine patients lacked these comorbidities, and they did not have other types of headaches. Patients were monitored for 1 year after the study protocol, but changes in their physical status and headaches were not detected. As a control group, 17 age- and sex-matched healthy subjects (15 females and 2 males, mean age  $\pm$  SD  $40.7 \pm 11.0$  years, age range 19-65 years) without headache and with a normal MRI were also prospectively enrolled in the study. Studies were performed in accordance with the approval of the Regional Research Ethics Committee of the Medical Center, Pécs.

Patients	Gender	Age (years)	Migraine Type	Disease Duration (years)	Attack Frequency (attack/month)	Chronic Disease†	Smoking	Locations of Voxels Containing WMHs
1	Female	19	With aura	5	3	Not known	No	L parietal
2	Female	25	Without aura	10	8	Not known	No	L occipital
3	Female	32	Without aura	14	2	Not known	No‡	R frontal
4	Female	38	Without aura	28	2.5	Not known	No	L frontal
5	Female	40	Without aura	20	3	Not known	No‡	R temporo-occipital
6	Male	41	Without aura	21	2	Not known	No	L frontal
7	Female	43	Without aura	25	10	Not known	No	L frontal
8	Female	43	With aura	24	1	Not known	No	R frontal
9	Female	44	Without aura	26	3.5	Not known	No	L frontal
10	Female	44	With aura	28	6	Not known	No	R frontal
11	Female	45	With aura	25	4	Not known	No‡	R frontal
12	Female	46	With aura	26	5	Not known	No	R frontal
13	Female	47	Without aura	25	8	Not known	No	L parietal
14	Female	50	Without aura	34	4	Not known	No	R frontal
15	Male	51	With aura	37	1	Not known	No	L frontal
16	Female	53	Without aura	35	2.5	Not known	No	L frontal
17	Female	65	With aura	45	.5	Not known	No	L frontoparietal

**Table 4.—Clinical Data of Migraine Patients With or Without Aura:** †Investigations included history taking, physical examinations, blood pressure measurements, serum, urine, and cerebrospinal fluid tests, transthoracic and transesophageal echocardiography to rule out the presence of hypertension, diabetes, thyroid gland dysfunction, homocysteinemia, hypercholesterinemia, hyperuricemia, oncological, hematological, and infectious diseases, vasculitis, multiple sclerosis, and cardiac embolization source.

‡Past history of smoking.

L = left; R = right; WMH = white matter hyperintensity.

### MRI Scanning Protocol and Image Analysis.

MRI was performed on a 3.0-Tesla clinical MRI scanner (Magnetom TIM Trio, Siemens Medical Solutions, Erlangen, Germany), with a field gradient strength of 40 mT/m and a 12 channel phased array head coil. The following MRI sequences were acquired: T1- and T2-weighted and 3-dimensional (3D) FLAIR images, diffusion-weighted images (DWIs) and perfusion-weighted images (PWIs), proton magnetic resonance spectroscopy (1H-MRS), and T1 and T2 relaxation time measurements.

*Identification of WMHs.*—WMHs were considered if visible as hyperintense on T2-weighted

and FLAIR images, without hypointensity on T1-weighted scans, and were larger than 3 mm. Only 1 WMH was investigated in each patient. The investigated WMHs' largest diameters ranged between 6 and 21 mm, and appeared in at least 3 consecutive slices (range between 3 and 10 slices) on 3D FLAIR images. All investigated WMHs were located in the supratentorial deep white matter.

*Imaging.*—Sagittal T1-weighted images were obtained using a fast low angle shot (FLASH) 2-dimensional (2D) sequence: TR/TE = 300/2.46 milliseconds, flip angle = 88°, 27 slices, slice thickness = 4 mm, 30% interslice gap, FOV = 220 x 220 mm<sup>2</sup>, matrix size = 256 x 320, receiver bandwidth = 330 Hz/pixel. For T2-weighted images, a turbo spin echo sequence was used: TR/TE = 6000/93 milliseconds, 30 slices, slice thickness = 4 mm, distance factor 20% (0.8 mm gap), FOV = 193 X 220 mm<sup>2</sup>, 280 x 320 pixel matrix, bandwidth = 220 Hz/pixel, number of echo trains 18. A turbo spin echo sequence was also used for the 3D FLAIR images: TR/TI/TE = 15,710/2750.8/105 milliseconds, 100 slices, slice thickness 1.5 mm, distance factor 0% (no gap), interleaved slice readout with 2 concatenation, FOV = 220 x 220 mm<sup>2</sup>, 192 x 192 pixel matrix, bandwidth = 400 Hz/pixel, number of echo trains 14. Diffusion was determined with a trace-weighted single-shot echo planar 2D imaging sequence: TR/TE = 4000/119 milliseconds, number of slices 20, slice thickness = 3.5 mm, distance factor 0% (no gap), FOV = 188 x 250 mm<sup>2</sup>, 144 x 192 mm<sup>2</sup> pixel matrix, FOV phase 75%, number of acquisitions 4, b values 0, 500, 1000 seconds/mm<sup>2</sup>. Perfusion images were acquired with a singleshot echo planar 2D sequence: TR/TE = 1400/33 milliseconds, flip angle = 68°, 20 slices, slice thickness = 3 mm, distance factor 33%, FOV = 210 x 210 mm<sup>2</sup>, 176 x 176 pixel matrix, bandwidth = 1150 Hz/pixel, fat saturation switched on. One hundred volumes were consecutively acquired, and contrast agent was administered after acquiring the 20th volume. A Medrad power injector was used for contrast agent and saline administration. A 0.1 mL/body weight amount gadopentetate dimeglumine (Magnevist, Bayer Schering Pharma AG, Berlin, Germany) was given at a 5

mL/second flow rate, and a 30-mL saline flush was used for washing in also at a 5 mL/second flow rate.

*Spectroscopy.*—Spectroscopy was performed before contrast agent administration to avoid any confounding effects on T1 and T2 relaxations. Before 1H-MRS acquisition, a voxel of 12 x 12 x 12 mm<sup>3</sup> was positioned on a preselected WMH. Two voxels were placed in every migraine patient: 1 in the selected WMH showing the radiological characteristics of the corresponding disease (WMH+ migraine voxel) (Table 4) and 1 in the contralateral, homotopic, NAWM area without MRI signal abnormality (WMH- migraine voxel) (Fig. 11). Two voxels were defined in each healthy subject according to the locations of the voxels of the age-matched migraine patient (healthy control voxels). Voxels were placed using T2 and 3D FLAIR images to position each voxel. After localized manual shimming and water suppression adjustment, fully relaxed short-echo time proton magnetic resonance spectra (point resolved spectroscopy sequence [PRESS], TR/TE = 6000/30 milliseconds, 128 accumulations, bandwidth = 1200 Hz, vector size 1024 points) were acquired. Water suppression was accomplished with a chemical shift-selective sequence pulse. At the end of the MRS acquisition, a reference water signal for the calibration of metabolite concentration was also acquired by turning off the water suppression. After acquiring the metabolite spectra, water signal T1 and T2 parameters were also determined. T1 was measured using the saturation recovery method. Six data points were collected, and only the TR was changed between each data point acquisition using the PRESS sequence: TR = 490, 900, 1400, 2000, 3000, and 4000 milliseconds; TE = 30 milliseconds, 1 accumulation, water signal suppression turned off, bandwidth = 2500 Hz, vector size = 1024, 4 preparation scans. T2 was obtained by measuring 6 data points with parameters differing only in echo times using the PRESS sequence: TR = 3000 milliseconds, TE = 30, 60, 90, 120, 180, and 240 ms, 1 accumulation, water signal suppression turned off, bandwidth: 2500 Hz, vector size = 1024, 4 preparation scans. The total experimental protocol lasted for 45.5 minutes in the following

order: (1) ~28 minutes for quantitative proton spectroscopy (with manual adjustments); (2) ~2.5 minutes for T1 measurement; (3) ~3 minutes for T2 measurement; (4) ~6.5 minutes for apparent diffusion coefficient (ADC) quantification; (5) ~1 minute for T2-weighted images; (6) ~3.5 minutes for 3D FLAIR; (7) ~2 minutes for perfusion.

*Data Processing.*—The T1 relaxation time for each voxel was calculated from the acquired water signals with different repetition times applying a standard exponential fit:

$$M = M0 * (1 - \exp(-TR/T1)) \quad (1)$$

where  $M$  is the actual signal intensity,  $M0$  is the signal intensity at thermal equilibrium, and TR is the repetition time.

The T2 relaxation time for each voxel was calculated from the acquired water signals with different echo times assuming a standard exponential signal decay:

$$M = M0 * \exp(-TE/T2) \quad (2)$$

where  $M$  is the actual signal intensity,  $M0$  is the signal intensity at thermal equilibrium, and TE is the echo time. Curve fittings were carried out on a Siemens Leonardo workstation using the Siemens spectroscopy software. Only Fourier transformation and phase correction on the measured signals were applied, no filters or any other corrections were used. The integral of the fitted water signal was used for the T1 and T2 fitting. To calculate the ADC values, freehand regions of interests (ROIs) were drawn on b0 images on the preselected WMHs. ROIs covered the WMHs selectively. Just like for the spectroscopy, a control area was also measured in the contralateral, homotopic NAWM. Within each ROI, the mean intensities for the b0, b500, and b1000 images were monoexponentially fitted using the following equation:

$$M = M0 * \exp(-b * ADC) \quad (3)$$

where  $M$  is the measured signal intensity in the presence of diffusion sensitization,  $M0$  is the signal intensity in the absence of diffusion sensitization,  $b$  is the b-value, and ADC is the ADC

value. Curve fitting and data analysis were performed using Matlab software (The MathWorks, Inc., Natick, MA, USA) for T1, T2, and ADC fittings. For metabolite quantitative analysis, spectroscopic raw data were postprocessed using the LCModel (Stephen Provencher Inc., Oakville, Ontario, Canada) [97]. The concentrations of N-acetyl-aspartate (NAA), glutamate/glutamine (Glx), creatine/phosphocreatine (Cr), choline (Cho), myo-inositol (mI), and lactate (Lac) were determined (Fig. 11). Perfusion analysis was performed on a Siemens Leonardo Workstation using Siemens Perfusion software (Siemens Medical Solutions, Erlangen, Germany). The relative cerebral blood flow (rCBF) and relative cerebral blood volume (rCBV) were calculated. The arterial input function was determined by an experienced radiologist. Freehand ROI analysis was performed. Lesions with a moderate T2 signal abnormality verified on T2, and FLAIR images could also be identified on the native, slightly T2- and T2\*-weighted raw ep2d images measured for perfusion analysis as high-intensity areas. ROIs were drawn on these raw ep2d images; afterwards, these ROIs were copied and used at the same slice of the calculated perfusion maps. The lesions and control areas to be measured as ROIs were selected and verified on T2 and FLAIR images in order to have a control contralateral white matter area without signal abnormality.

**Statistical Analysis.**—All statistical tests were performed by the IBM SPSS Software (version 19, SPSS, Inc., Chicago, IL, USA). To test normality, the Kolmogorov–Smirnov and Shapiro–Wilk tests were applied. Because the variables did not follow the normal distribution, non-parametric tests were used in subsequent analysis. The Kruskal–Wallis and Mann–Whitney *U*-tests were utilized to detect any significant differences in each variable obtained from WMH+ migraine, WMH- migraine and healthy control voxels. For comparisons, 17 voxel values were used in the healthy control group according to the locations of WMH+ migraine voxels. For T1 and T2 time measurements as well as perfusion analysis, the data of 15 migraine patients and 15

healthy subjects were used, as 2 patients could not complete the MRI study. Patients with and without aura were compared with each other to assess the possible differences between the 2 groups. The level of statistical significance was set at 0.05.

### III.3 Results

There was no statistical difference between the migraine subgroups regarding the MRI findings; consequently, all the measured data were used in 1 group.

**Diffusion Analysis.**—The ADC values were significantly higher in the WMH+ migraine voxels than in both the NAWM voxels of migraineurs ( $P < .001$ ; Table 5, Fig. 12A) and in the healthy control voxels ( $P < .001$ ; Table 5, Fig. 12A). A statistical difference was not found between the WMH- migraine voxel group and the healthy control voxel group (Table 5, Fig. 12A).

**T1 and T2 Relaxation Time Measurements.**— Although the T1 relaxation time was more prolonged in the WMH+ migraine voxel group than in the WMH- migraine and control subject voxel groups, the differences were not significant statistically (Table 5, Fig. 12B). Higher T2 time values were found in the WMH+ migraine voxels as compared with the WMH- migraine ( $P < .002$ ; Table 5, Fig. 12B) and the healthy control subject voxels ( $P < .002$ ; Table 2, Fig. 3B). The statistical analysis did not show significant differences regarding T1 and T2 relaxation times between the WMH- voxel and the healthy control subject groups (Table 5, Fig. 12B).

**Table 5: - Results of the Measured Variables and the Statistical Analyses**

	WMH+ migraine voxel group (voxel number = 17†)			WMH- migraine voxel group (voxel number = 17†)			Healthy control voxel group (voxel number = 17†)			Statistics			
	Median	25th percentile	75th percentile	Median	25th percentile	75th percentile	Median	25th percentile	75th percentile	M-W test WMH+ vs WMH-	M-W test WMH+ vs control	M-W test WMH- vs control	K-W test
ADC (mm <sup>2</sup> /second)	9.39	8.37	10.75	6.64	6.29	6.92	6.21	5.76	6.67	<i>P</i> < .001***	<i>P</i> < .001***	<i>P</i> = .085	<i>P</i> < .001***
T1 (milliseconds)	1057.00	983.60	1180.00	1019.00	969.60	1176.00	1006.00	964.00	1031.75	<i>P</i> = .412	<i>P</i> = .069	<i>P</i> = .390	<i>P</i> = .191
T2 (milliseconds)	79.00	74.82	89.13	70.01	65.57	74.26	70.30	62.75	75.32	<i>P</i> = .002**	<i>P</i> = .002**	<i>P</i> = .682	<i>P</i> = .003**
NAA (mmol/L)	8.13	6.62	8.69	8.56	8.23	9.63	8.66	7.98	9.34	<i>P</i> = .031*	<i>P</i> < .016*	<i>P</i> = .999	<i>P</i> = .031*
Glx (mmol/L)	8.55	7.31	9.03	8.66	7.17	10.91	7.76	6.92	9.90	<i>P</i> = .610	<i>P</i> = .760	<i>P</i> = .433	<i>P</i> = .703
Cho (mmol/L)	1.54	1.28	1.82	1.74	1.46	1.90	1.63	1.32	1.74	<i>P</i> = .218	<i>P</i> = .865	<i>P</i> = .218	<i>P</i> = .342
Cr (mmol/L)	4.77	4.39	5.27	5.63	5.26	5.96	5.61	5.24	5.83	<i>P</i> = .001**	<i>P</i> = .002***	<i>P</i> = .683	<i>P</i> = .001**
mI (mmol/L)	4.81	4.13	5.23	4.53	3.91	4.99	4.86	4.30	6.16	<i>P</i> = .563	<i>P</i> = .375	<i>P</i> = .160	<i>P</i> = .336
rCBF	47.00	32.00	71.50	59.00	39.50	89.00	55.00	38.25	76.75	<i>P</i> = .139	<i>P</i> = .589	<i>P</i> = .449	<i>P</i> = .362
rCBV	198.00	150.00	218.00	236.00	176.00	329.00	204.00	162.00	243.50	<i>P</i> = .098	<i>P</i> = .682	<i>P</i> = .176	<i>P</i> = .202

\* *P* < .05, \*\* *P* < .01, \*\*\* *P* < .001.

†Fifteen migraine patients' and healthy subjects' data were used for the statistical analysis of the T1 and T2 relaxation times, and the rCBF and rCBV measurements.

Because the measured variables did not follow the normal distribution, the data are represented by their median, and 25th and 75th percentile values. Only the significant differences are marked by the respective *P* values in the statistical section.

ADC = apparent diffusion coefficient; Cho = choline; Cr = creatine/phosphocreatine; Glx = glutamate/glutamine; K-W test = Kruskal-Wallis test; mI = myo-inositol; M-W test = Mann-Whitney test; NAA = N-acetyl-aspartate; rCBF = relative cerebral blood flow; rCBV = relative cerebral blood volume; WMH = white matter hyperintensity.

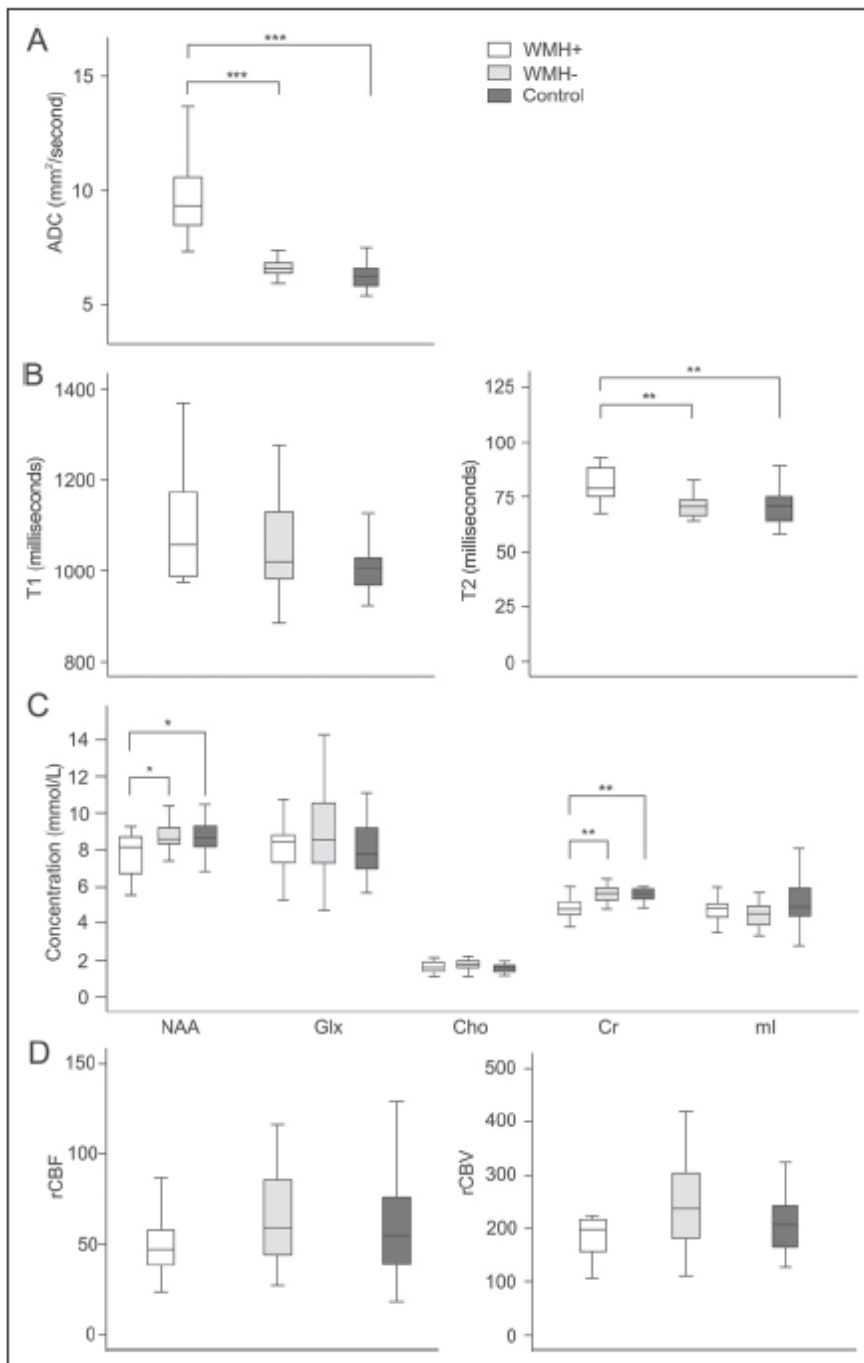


**Fig 12.**—Results and comparisons of apparent diffusion coefficient (ADC) values (A), T1 and T2 relaxation times (B), brain metabolite concentrations (C), and relative cerebral blood flow BF) and relative cerebral blood volume (rCBV) values (D) measured in a 12x12x12 mm single voxel in the white matter of migraine patients containing the signal abnormality in the migraine patients' contralateral, normal-appearing white matter and in the white matter of healthy control subjects. The statistically significant differences between the groups are shown by \* on the figures (\* $P < .05$ , \*\* $P < .01$ , \*\*\* $P < .001$ ). NAA = N-acetylaspartate; Glx = glutamate/glutamine; Cho = choline, Cr: creatine/phosphocreatine, ml: myo-inositol; WMH = white matter hyperintensity

**<sup>1</sup>H-MRS Studies.**—The NAA and Cr concentrations in the WMH+migraine voxels were significantly decreased as compared with both the WMHmigraine (NAA  $P = .031$ , Cr  $P = .001$ ; Table 5, Fig. 12C) and healthy control voxels (NAA  $P = .016$ , Cr  $P = .002$ ; Table 5, Fig. 12C). Comparisons of other metabolites did not show a statistical difference among the 3 voxel groups (Table 5, Fig. 12C). A Lac peak was not detected in the study.

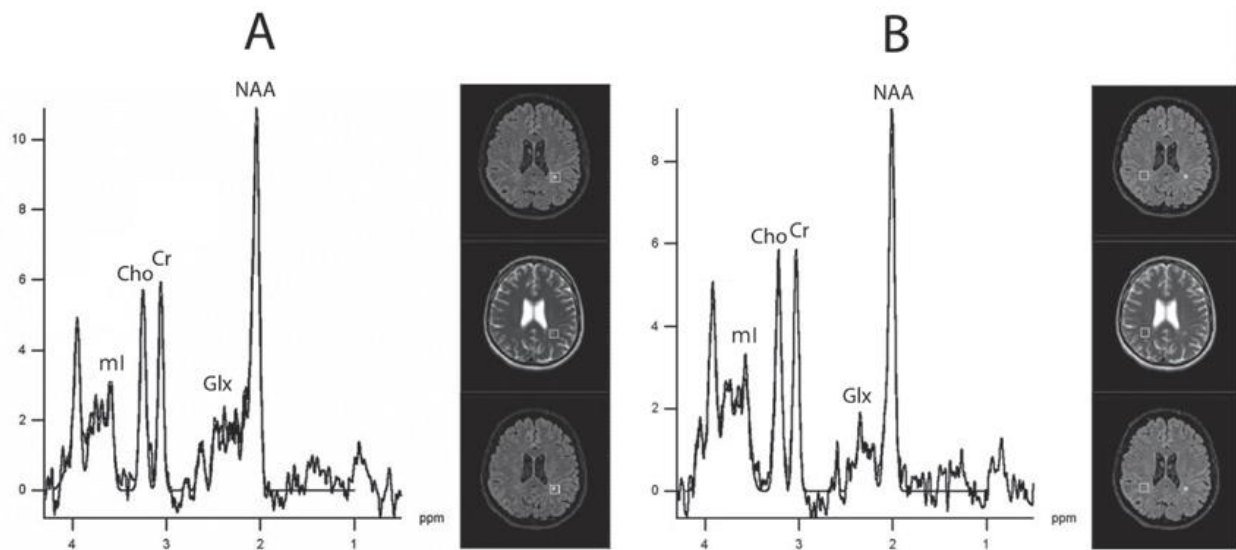


**Fig 13.**—Comparative qualitative proton magnetic resonance spectra from brain white matter containing hyperintensity (A) and from the contralateral normal-appearing white matter (B) of a 38-year-old patient with migraine without aura measured with a point resolved spectroscopy sequence (TR/TE: 6000/30 milliseconds). Qualitatively, only slight metabolite changes are visible, while quantitative approach revealed significant metabolite alterations. The right side of the image represents the left side of the brain. Cho = choline; Cr = creatine/phosphocreatine; Glx = glutamate/glutamine; mI = myo-inositol; NAA = N-acetyl-aspartate.

**Perfusion Analysis.**—In the WMH+ migraine voxel group, all rCBF and rCBV values were lower than in both the WMH- migraine voxel group and in the healthy control voxel group; however, the differences did not reach the level of statistical significance (Table 5, Fig. 12D).

### III. 4. Discussion

We have examined chronic migraine-related supratentorial WMHs with different quantitative MRI techniques in the present study. We found significantly higher ADC values, prolonged T2 relaxation times, decreased NAA and Cr concentrations in the WMHs, while the T1 relaxation times were mildly prolonged. Although the intralesional rCBF and rCBV values were lower in all the examined patients than in the control white matter areas, these differences were not statistically significant. Differences were not found between the NAWM of migraineurs and the healthy subjects' white matter.

**Evaluation of MRI Data in Migraine.**—Several functional MRI studies have been performed in migraine in different ictal states [91], but these studies did not focus specifically on the investigation of WMHs; therefore, the quantity of available data is limited. DWI detects changes in the movement of water across neuronal membranes in different brain disorders with morphological abnormalities [98]. Alterations of the microdynamics of cellular transport between subcompartments may change diffusivity [98]. We detected increased ADC values in the WMHs in our diffusion analysis. This finding represents elevated levels of random water molecule motion inside the WMHs and can be the consequence of tissue damage [98]. In vivo measurements of T1 and T2 relaxation times of protons provide information about the tissue water environment [99]. We measured mildly prolonged T1 and more prolonged T2 time values in the WMHs of migraine patients. These alterations can represent an increased extracellular water fraction based on a less bound state of water in the damaged tissue similar to other chronic diseases [100,101]. Further, the presence of an increased free water fraction is also supported by the higher ADC values [102] detected in the WMHs. <sup>1</sup>H-MRS suppresses the high background signals to measure the concentration of the major brain neurotransmitters and metabolites [102]. We found decreased NAA and Cr concentrations in the WMHs. NAA is a neuronal and

axonal marker, and its low concentration may reflect decreased axonal viability, function, and cell loss in the white matter [102]. Cr is a single resonance containing creatine and phosphocreatine, and the concentrations of these metabolites are higher in astrocytes and oligodendrocytes than in neurons [102-104]. The decreased brain levels of Cr can reflect tissue degeneration with a low cellularity and less efficient mitochondrial functioning [102-104]. Levels of other examined metabolites (Glx, Cho, mI) were normal in the WMHs, and Lac was not present. These findings do not indicate cell loss, myelin breakdown, remyelination, astrogliosis, or the presence of anaerobic glycolysis [102-105]. PWI is a gadolinium-based functional MRI technique that allows the measurement of capillary perfusion by rapid image acquisition [98]. We found mildly reduced intralesional rCBF and rCBV values in all investigated migraine patients. In chronic tissue damage, the decreased perfusion can reflect axonal and cellular loss, with a lower oxygen use, lower blood flow demand, and subsequent CBF decrease [98].

#### **MRI Studies in Other Diseases With WMHs.—**

WMHs can be detected not just in migraine but also in other diseases, such as multiple sclerosis, ischemic stroke, silent brain white matter lesions, and tension-type headache [82,85,92,94]. Disease-specific differentiation of these lesions is not possible in all cases with conventional MRI without histopathological analysis [92,94]. Using nonconventional MRI techniques, both the inactive, chronic multiple sclerosis plaques, and the ischemic lesions are characterized by tissue destruction with reduced axonal and glial cell density, enlargement of the extracellular space, and an increased free water fraction, decreased tissue blood perfusion, and the lack of anaerobic glycolysis [95,103-111]. In multiple sclerosis lesions, signs of ongoing myelin breakdown or remyelination can be seen in the isointense plaques, and astrogliosis is present [103,104,106-108]. Previous studies have shown that most of the asymptomatic WMHs are linked to chronic low-grade ischemia in the elderly [100,102]. Compared with chronic white

matter infarctions, the functional MRI measurements of silent brain white matter lesions demonstrated similar but less severe tissue affection [100,112,113]. In the primary headache group, brain white matter lesions occur not just in migraine but also in patients with tension-type headache[82,85]. This finding indicates that both migraine and tension-type headache may be associated with early pathological changes in the brain and may share, at least in part, common pathogenic pathways [82,85].

**Proposed Pathomechanisms Leading to the Evolution of WMHs in Migraine.**—There are suggestions that WMHs are the consequence of a microvascular ischemic disturbance. These abnormalities have been interpreted as an indirect marker of focal cerebral hypoperfusion induced by migraine attacks [88,114,115]. Repeated and prolonged oligemia during and after migraine attacks may affect the vulnerable small deep penetrating arteries, and the reduced local perfusion may lead to minor brain injury revealed as white matter lesions [88,114,115]. The cortical spreading depression, which is present in all migraine phenotypes, indirectly alters the blood–brain barrier’s permeability through a matrix metalloproteinase-9-dependent cascade activation and can lead to white matter cellular injury caused by ischemia with glutamatergic excitotoxicity and intracellular calcium-mediated apoptosis [79,116]. The local release of vasoactive neuropeptides could result in further changes in cerebral hemodynamics [117]. Migraine may also associate with endothelial dysfunction and oxidative stress because of increased nitric oxide levels during attacks [118,119]. If the endothelial changes are accompanied with platelet aggregation, this process may lead to microvascular brain damage [118,119]. Reversible vasoconstriction of cerebral arteries can also cause transient or permanent focal neurological deficits with or without ischemic lesions during headache [120].

**Study Limitations.**—We are aware that the present study has some limitations, such as the small patient population because of the strict inclusion criteria and that the voxels contained not just the WMHs but perilesional white matter in different proportions, as well. The small sample

size does not allow to control for potential confounding factors or to investigate the possible differences between the migraine subgroups. It also limits the generalizability of the measured data.

### **III. 4 Conclusions**

The quantitative MRI measurements of chronic WMHs in migraine patients demonstrated tissue damage with axonal loss, glial hypocellularity, an enlarged extracellular space, and an increased extracellular water fraction. Signs of myelin breakdown, astrogliosis, and anaerobic glycolysis were not present. These abnormalities are similar to those detected in chronic ischemic stroke and in silent brain white matter lesions with ischemic origin. Our findings may indicate that the WMHs can be the consequence of a microvascular ischemic disturbance in migraine.

## **IV. Quantitative MRI Analysis of the Brain after Twenty-Two Years of Neuromyelitis Optica Indicates Focal Tissue Damage**

### **IV. 1. Introduction**

Neuromyelitis optica (NMO) is an inflammatory demyelinating disorder of the central nervous system characterized by relapsing optic neuritis and transverse myelitis. Anti-AQP4 antibodies have been identified in the sera in 60–90% of cases [121] . Conventional brain magnetic resonance imaging (MRI), i.e. T1-weighted, T2-weighted or fluid-attenuated inversion recovery (FLAIR), is usually normal in NMO. Longitudinal studies, however, have indicated signal alterations in almost 80% of cases, and with diffusion-weighted imaging (DWI) an increased diffusivity has been observed. These suggest chronic tissue damage [122] . Previously, a few studies investigated ‘normal appearing white matter’ (NAWM) by MR spectroscopy in NMO and suggested no metabolite alteration in patients with a mean duration of disease below 8 years [123,124] . Here, by using a multimodal MRI approach, we examined diffusivity and quantitative metabolite changes in the NAWM of the brain after a long duration (22years) of NMO.

### **IV.2 .Case Report and Methods**

The regional ethical committee and the patient approved the study. This female patient developed bilateral optic neuritis (ON) at the age of 8 years. Despite treatment with azathioprine, ON relapsed 4–5 times annually. Four years later severe myelitis developed. MRI indicated longitudinally extensive transverse myelitis. Myelitis relapsed at least 10 times in the

next 3 years. Anti-AQP4 antibodies were identified in the sera by a cell-based assay (Euroimmune, Lübeck, Germany) when the patient was 29 years old.

Quantitative MRI data obtained from 20 age-matched ( $30 \pm 10$  years) healthy volunteers were used as a control for diffusion and spectroscopic analysis, measured with the same sequences and parameters. Three patients were also included with short-term (3-, 4- and 5-year duration, respectively) anti-AQP4-seropositive NMO and no brain lesion on conventional MRI.

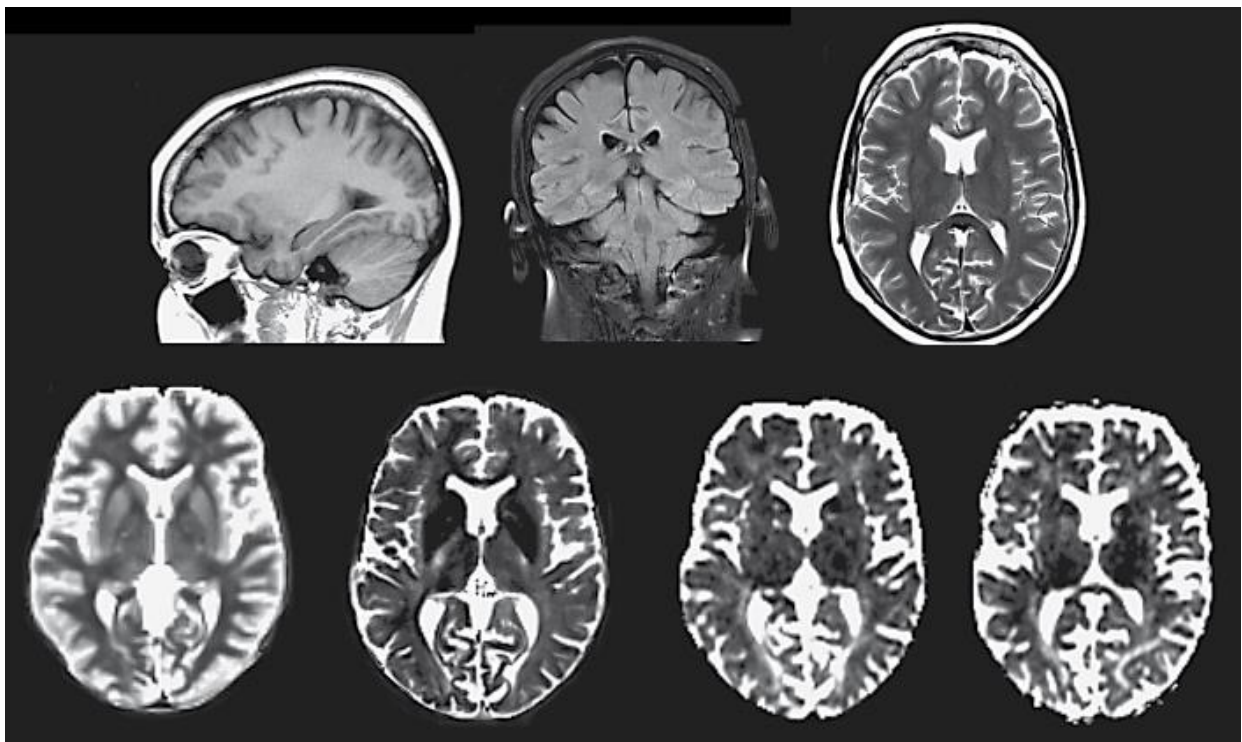


**Fig. 14.** Brain MRI after 22 years of disease duration. Conventional MRI measures showed no abnormalities as indicated on representative sagittal T1-weighted ( **a** ), coronal FLAIR ( **b** ) and axial T2-weighted ( **c** ) sequences. The T1 map ( **d** ) and T2 map ( **e** ) suggested altered relaxivity. The ADC map indicated white matter lesions with high diffusivity at the same time ( **f** ) and 6 months later ( **g** ).

MRI was performed on a 3.0 T clinical MRI scanner (Siemens Magnetom TIM Trio). The following sequences were measured: T1-weighted imaging [repetition time/echo time (TR/TE) = 300/2.5 ms, twenty-seven  $0.9 \times 0.7 \times 4$  mm sagittal slices], T2-weighted imaging (TR/TE =

6,000/74 ms, thirty  $0.7 \times 0.7 \times 4$  mm axial slices), FLAIR imaging (TR/TI/TE = 5,000/1,800/93 ms, thirty-four  $0.9 \times 0.9 \times 4$  mm coronal slices), 3-dimensional T1- weighted contrast-enhanced imaging (TR/TI/TE = 900/1,760/3.4ms, flip angle  $9^\circ$ , ten  $0.9 \times 0.9 \times 1.5$  mm axial slices, 0.1 ml/kg Magnevist ® contrast agent), DWI (TR/TE = 5,923/128 ms, twenty-five  $1.3 \times 1.3 \times 3.5$  mm axial slices, b value = 0, 500, 1,000, 2,000, 3,000, 4,000, 5,000 s/mm<sup>2</sup> ), T1 measurement with inversion recovery TSE sequence (TR/TE/TI: 4,000/8/100, 300, 700, 1,200, 1,500, 2,100 ms,  $1.6 \times 1.6 \times 4$  mm axial slices), T2 measurement with Carr-Purcell-Meiboom-Gill sequence (TR/TE: 20, 40, 60, 80, 100, 120, 140, 160, 180, 200 ms,  $1.1 \times 1.1 \times 5$  mm axial slices) quantitative proton spectroscopy (TR/TE = 6,000/30 ms, 128 accumulations, position-resolved spectroscopy sequence), T1, T2 and diffusion parameter fittings were performed. The regions of interest used for biexponential diffusion analysis were selected according to apparent diffusion coefficient (ADC) abnormalities and were drawn on monoexponential ADC maps: 10 white matter areas with normal and elevated diffusivity, respectively, were selected throughout the whole brain. The same regions were evaluated by the control group. For T1 and T2 analysis, no control group was measured, i.e. only the white matter of the patient was analyzed by placing regions of interest on quantitative maps of 10 well-defined altered relaxivity areas and 10 NAWM areas. Quantitative proton spectroscopy data were processed with LC model. Four voxels were analyzed in the white matter ( $12 \times 12 \times 12$  mm<sup>3</sup>): 3 voxels were positioned on high diffusivity areas and 1 voxel in an area with normal diffusivity. MRI analyses were performed twice, with an interval of half a year.

For statistical comparison of quantitative parameters, the Mann-Whitney test was used. Spectroscopic data of 3 lesions was also compared to the healthy control group in order to observe the tendencies of metabolite alterations, despite the low statistical power.

### IV.3 Results

**Table 6.** Quantitative MRI parameters of gray and white matter after in a patient with NMO of 22-year duration

	Quantitative diffusion, T1 and T2 parameters			
	NAWM control <sup>a</sup>	NAWM patient <sup>b</sup>	Lesion patient <sup>b</sup>	p values <sup>c</sup>
ADC	6.3±0.6	6.3±0.4	8.5±0.5	<0.0001
ADCfast	12.3±1.7	11.2±0.7	14.1±0.1.1	<0.0001
ADCslow	1.0±0.5	1.1±0.4	1.4±0.5	n.s.
pfast	67.2±4.5	68.9±02.6	76.7±1.3	<0.0001
pslow	32.8±4.5	31.6±2.6	23.3±1.3	<0.0001
T1, ms		688.1±27	767.8±35	<0.0001
T2, ms		86.4±5	100.1±9	<0.0007

	Quantitative spectroscopic measurements				
	WM lesion patient <sup>d</sup>	Contralateral NAWM, patient <sup>d</sup>	WM lesion average	Healthy control WM	p values <sup>e</sup>
NAA	7.8	10.1	7.7±0.7	9.0±1.1	<0.05
Cr	5.8	5.1	5.4±0.3	5.7±0.6	n.s.
Cho	1.6	1.4	1.6±0.1	1.6±0.2	n.s.
Ins	6.8	5.6	6.9±0.8	4.5±1.0	<0.001
Glx	11.1	6.3	8.0±2.5	8.5±2.0	n.s.

All data are presented in mean ± SD format. All metabolite concentrations are shown in mmol/l. ADCfast and ADCslow are the ADC values (mm<sup>2</sup>/s\*10<sup>-4</sup>), pfast and pslow are the percentages of the fast- and slow-diffusing water fractions. NAA: N-acethyl aspartate; Ins: myo-inositol; Glx: glutamine, glutamate; Cho = choline; Cr = creatin; n.s. = nonsignificant; WM = white matter.

*a* Diffusion parameters were measured throughout the whole white matter in 20 age-matched healthy controls.

*b* Regions of interest for quantitative diffusion analysis, T1 and T2 measurements were selected according to ADC and relaxation abnormalities (lesions), and drawn on quantitative parameter maps: 10 normal and 10 altered white-matter areas were selected throughout the whole brain according to the control group.

*c* Lesions vs. NAWM of patient.

*d* White-matter lesion and the corresponding contralateral NAWM were measured as indicated by the quantitative maps.

*e* The average of 3 lesions measured by single voxel quantitative spectroscopy were compared to 20 healthy controls.

On T1, T2, FLAIR and post-contrast 3-dimensional T1 sequences, no signal abnormalities were detected. Nevertheless, ADC T1 and T2 maps identified white matter lesions with high ADC values and altered relaxation properties (Fig. 14 ). In the quantitative analysis of 10 hyperintense

areas compared with 10 NAWM areas based on the ADC map, both mono- and biexponential diffusion showed significant differences: data indicated an increased monoexponential ADC value, an increased percentage of the fast-diffusing water fraction and an increased ADC value of the fast fraction (Table 6). T1 and T2 parameters were also significantly elevated in these patchy areas compared to NAWM. When the 10 NAWM regions of the patient were compared to the white matter of 20 healthy subjects, only the ADC of the fast fraction appeared to be somewhat lower ( $p = 0.02$ ) (Table 6).

Such patchy alterations were not detectable in the NAWM of the 3 cases with short-term NMO (Fig. 15) . Comparative spectroscopic measurement in an area where quantitative maps suggested altered diffusivity and relaxation times showed decreased N-acetyl aspartate (NAA) and elevated myoinositol (Ins) and glutamine and glutamate (Glx) levels when compared to the corresponding contralateral white-matter area with unaltered quantitative features (Table 6). When the 3 voxels positioned on lesions were compared to the healthy controls, the NAA was significantly lower, while Ins was elevated (Table 6). The NAWM of patients with short-term NMO did not show significant differences compared to the healthy controls. Repeated MRI analysis performed after 6 months identified patchy alterations in the same regions in the patient with long-term NMO (Fig. 14).

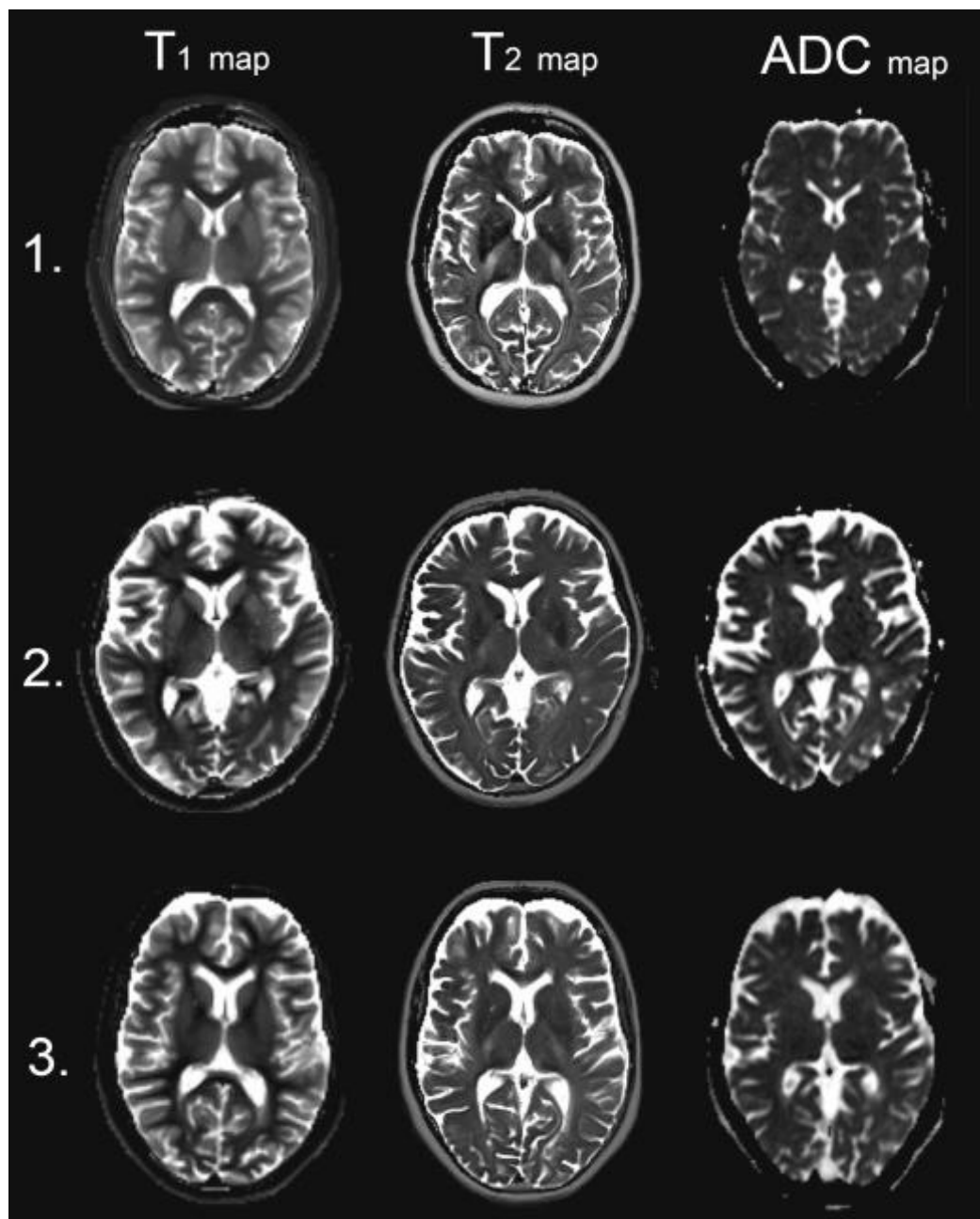


*Fig. 15. Brain MRI in 3 patients with short-term NMO. Quantitative T1, T2 and ADC maps indicated no patchy white matter areas with elevated diffusivity and T1–T2 relaxation time in patients with short-term NMO. Duration of disease is shown at 3 years (1), 4 years (2) and 5 years (3).*

## IV. 5. Discussion

Despite the long duration (22 years) of NMO, routine T1 and T2 imaging of the brain tissue appeared to be normal in this patient. In contrast, ADC values were significantly higher in several areas of the NAWM, which may indicate focal tissue damage even in brain areas not characterized by high expression of AQP4, as already indicated [122]. The b-value range was extended to get more insight into the diffusion changes: extension of the b-value range helps to identify two water populations, fast and slow-diffusing water molecules. NAWM areas with high ADC values are characterized by predominance of the fast-diffusing water component, similar to extracellular edema [125]. T1 and T2 parameter times were also elevated, which is in good agreement with the increase in the fast-diffusing water content. The change is around 10–15%, which gives poor contrast on T1- and T2-weighted images and therefore can be classified as NAWM. Previous nonquantitative proton spectroscopy of NAWM showed normal metabolite ratios [123, 124]. Here, we quantitatively measured metabolite concentrations by using short TE along with long TR to minimize the T1 and T2 weighting in the spectra, in contrast to previous studies. In these analyses, we did not measure the metabolite relaxation times due to our limited time resources but as changes in the water T1 and T2 relaxation times in our study suggest differences, the short TR (1,500–2,000ms) and long TE (TE: 135ms) used in previous studies may be inappropriate, since such differences can be masked. In our measurements, the abnormal NAWM area that appeared to have altered quantitative MR parameters also showed decreased NAA and increased Ins compared to the corresponding contra lateral NAWM area. The voxels positioned within hyperintense areas on the ADC map and compared to the healthy controls also showed the same distribution of metabolites. The metabolite changes within the areas of altered diffusivity and T1 and T2 relaxation times together may refer to axonal loss and tissue degeneration in areas after 22 years, which persist for at least 6 months. Such alterations could

not be identified in the 3 cases with short-term NMO. In addition, the distribution and volume of the patchy alterations were more extensive than incidental brain lesions indicated in other patients; of note, no white matter lesions were obvious on conventional MRI. Such pathology of abnormal NAWM could hardly be due to only secondary alterations caused by myelitis, and may rather indicate primary pathology of the white and grey matter as also suggested by other observations [122] . In conclusion, our multimodal, combined MRI approach in a case of long-lasting NMO indicated: (1) normal findings on conventional MRI; however, (2) thorough quantitative MRI analysis clearly showed extensive patchy areas in NAWM showing altered diffusion and relaxational features in contrast to short-term NMO, (3) within such abnormal NAWM areas, definite metabolite changes suggested axonal loss and tissue degeneration when compared quantitatively to NAWM, (4) such alterations in diffusivity and metabolite concentrations persisted for at least 6 months; nevertheless, (5) the MRI morphology was fundamentally different from long-lasting MR spectroscopy and other incidental lesional findings, and thus may suggest different pathological processes.

## V. PEER-REVIEWED PUBLICATIONS OF THE AUTHOR

### The thesis is based on the following publications:

1: **Aradi M**, Koszegi E, Orsi G, Perlaki G, Trauninger A, Toth A, Schwarcz A, Illes Z. Quantitative MRI Analysis of the Brain after Twenty-Two Years of Neuromyelitis Optica Indicates Focal Tissue Damage. *Eur Neurol.* 2013 Jan 10;69(4):221-225.

2: **Aradi M**, Schwarcz A, Perlaki G, Orsi G, Kovács N, Trauninger A, Kamson DO, Erdélyi-Bótor S, Nagy F, Nagy SA, Dóczi T, Komoly S, Pfund Z. Quantitative MRI Studies of Chronic Brain White Matter Hyperintensities in Migraine Patients. *Headache.* 2012 Dec 26. doi: 10.1111/head.12013.

3: **Aradi M**, Steier R, Bukovics P, Szalay C, Perlaki G, Orsi G, Pál J, Janszky J, Dóczi T, Schwarcz A., Quantitative proton MRI and MRS of the rat brain with a 3T clinical MR scanner. *J Neuroradiol.* 2010 Mar 22.

### Other publications:

1: Steier R, **Aradi M**, Pál J, Perlaki G, Orsi G, Bogner P, Galyas F, Bukovics P, Janszky J, Dóczi T, Schwarcz A.: A biexponential DWI study in rat brain intracellular oedema. *Eur J Radiol.* 2012 Aug;81(8):1758-65.

2: Steier R, **Aradi M**, Pál J, Bukovics P, Perlaki G, Orsi G, Janszky J, Schwarcz A, Sulyok E, Dóczi T. The influence of benzamil hydrochloride on the evolution of hyponatremic brain edema as assessed by in vivo MRI study in rats. *Acta Neurochir (Wien).* 2011

Oct;153(10):2091-7;

3: Nagy SA, **Aradi M**, Orsi G, Perlaki G, Kamson DO, Mike A, Komaromy H, Schwarcz A, Kovacs A, Janszky J, Pfund Z, Illes Z, Bogner P., Bi-exponential diffusion signal decay in normal appearing white matter of multiple sclerosis. *Magn Reson Imaging*. 2013 Feb;31(2):286-95.

4: Cselik Z, **Aradi M**, von Jako RA, Lelovics Z, Juhász I, Egyházi Z, Bogner P, Repa I, Schwarcz A. Impact of infrared laser light-induced ablation at different wavelengths on bovine intervertebral disc ex vivo: evaluation with magnetic resonance imaging and histology. *Lasers Surg Med*. 2012 Jul;44(5):406-12.

5: Szalay C, **Aradi M**, Schwarcz A, Orsi G, Perlaki G, Németh L, Hanna S, Takács G, Szabó I, Bajnok L, Vereczkei A, Dóczi T, Janszky J, Komoly S, Örs Horváth P, Lénárd L, Karadi Z. Gustatory perception alterations in obesity: an fMRI study. *Brain Res*. 2012 Sep 14;1473:131-40.

6: Toth A, Kovacs N, Perlaki G, Orsi G, **Aradi M**, Komaromy H, Ezer E, Bukovics P, Farkas O, Janszky J, Doczi T, Buki A, Schwarcz A. Multi-modal magnetic resonance imaging in the acute and sub-acute phase of mild traumatic brain injury: can we see the difference? *J Neurotrauma*. 2013 Jan 1;30(1):2-10.

7: File G, Bajzik G, Dóczi T, Orsi G, Perlaki G, Lelovics Z, **Aradi M**, Schwarcz A. Brain tissue water content determination based on T1 relaxation time of water and quantitative cerebral <sup>1</sup>H MRS at 3T using water as an internal reference. *Ideggyogy Sz*. 2012 Sep 30;65(9-10):325-32.

8: Kamson DO, Illés Z, **Aradi M**, Orsi G, Perlaki G, Leél-Óssy E, Erdélyi-Botor S, Pótó L, Trauninger A, Pfund Z. Volumetric comparisons of supratentorial white matter hyperintensities on FLAIR MRI in patients with migraine and multiple sclerosis. *J Clin Neurosci*. 2012 May;19(5):696-701.

9: Vereczkei A, Szalay C, **Aradi M**, Schwarcz A, Orsi G, Perlaki G, Karádi Z, Németh L, Hanna S, Takács G, Szabó I, Bajnok L, Mohos E, Lénárd L, Dóczi T, Janszky J, Komoly S, Horváth OP. Functional MRI investigation of brain activity triggered by taste stimulation. *Magy Seb*. 2011 Dec;64(6):289-93.

10: Móricz P, Kiss P, Somogyvári K, **Aradi M**, Gerlinger I. Objective assessment of olfactory rehabilitation after laryngectomy. *Clin Otolaryngol*. 2011 Oct;36(5):518-9.

11: Orsi G, Perlaki G, Kovacs N, **Aradi M**, Papp Z, Karadi K, Szalay C, Karadi Z, Lenard L, Tenyi T, Plozer E, Gabriel R, Nagy F, Doczi T, Komoly S, Jokeit H, Schwarcz A, Janszky J. Body weight and the reward system: the volume of the right amygdala may be associated with body mass index in young overweight men. *Brain Imaging Behav*. 2011 Jun;5(2):149-57.

12: Horváth RA, Schwarcz A, **Aradi M**, Auer T, Fehér N, Kovács N, Tényi T, Szalay C, Perlaki G, Orsi G, Komoly S, Dóczi T, Woermann FG, Gyimesi C, Janszky J. Lateralisation of non-metric rhythm. *Laterality*. 2011 Sep;16(5):620-35

13: Trauninger A, Leél-Ossy E, Kamson DO, Pótó L, **Aradi M**, Kövér F, Imre M, Komáromy H, Erdélyi-Botor S, Patzkó A, Pfund Z. Risk factors of migraine-related brain white matter hyperintensities: an investigation of 186 patients. *Pain*. 2011 Feb;12(1):97-103

14: Auer T, Schwarcz A, **Aradi M**, Kalmár Z, Pendleton C, Janszky I, Horváth RA, Szalay C, Dóczi T, Komoly S, Janszky J. Right-left discrimination is related to the right hemisphere. *Laterality*. 2008 Sep;13(5):427-38

15: Bajzik G, Auer T, Bogner P, **Aradi M**, Kotek G, Repa I, Doczi T, Schwarcz A Quantitative brain proton MR spectroscopy based on measurement of the relaxation time T1 of water.. *J Magn Reson Imaging*. 2008 Jul;28(1):34-8

16: Auer T, Barsi P, Bone B, Angyalosi A, **Aradi M**, Szalay C, Horvath RA, Kovacs N, Kotek G, Fogarasi A, Komoly S, Janszky I, Schwarcz A, Janszky J. History of simple febrile seizures is associated with hippocampal abnormalities in adults. *Epilepsia*. 2008 Sep;49(9):1562-9

17: Auer T, Schwarcz A, Ezer E, Czeiter E, **Aradi M**, Hudvágner S, Janszky J, Büki A, Dóczi T. Diffusion tensor and functional MR imaging of severe traumatic craniocerebral injury at low magnetic field. *Ideggyogy Sz*. 2007 Nov 30;60(11-12):480-8

## References:

- [1]. Immanuel Estermann; Otto Stern, Magnetic deflection of hydrogen molecules and the magnetic moment of the proton. II), Zeitschrift für Physik 85, 17-24 (1933)
- [2]. I.I. Rabi, J.R. Zacharias, S. Millman, P. Kusch (1938). "A New Method of Measuring Nuclear Magnetic Moment". Physical Review 53 (4): 318–327.
- [3]. Purcell, E.; Torrey, H.; Pound, R. (1946). "Resonance Absorption by Nuclear Magnetic Moments in a Solid". Physical Review 69: 37
- [4]. F. Bloch, "Nuclear Induction," Phys. Rev. 70, 460 (1946); F. Bloch, W.W. Hansen, and M. Packard, "The Nuclear Induction Experiment," Phys. Rev. 70, 474 (1946).
- [5]. Hahn EL. Spin echoes. Bull. Amer. Phys. Soc. 24:13, 1949
- [6]. G. Neil Holland MPhil, James R. Macfall PhD, An overview of digital spectrometers for MR imaging, JMRI, Vol.2, Issue 2, pages 241–246, March/April 1992
- [7]. Proksa R. A fully digital spectrometer for low field MR imaging systems (abstr). In: Book of abstracts: Society of Magnetic Resonance in Medicine 1988. Berkeley. Calif Society of Magnetic Resonance in Medicine, 1988; 266.
- [8]. Raymond Damadian, Tumor Detection by Nuclear Magnetic Resonance, Science 19 March 1971: Vol. 171 no. 3976 pp. 1151-1153;
- [9]. Raymond Damadian, Ken Zaner, Doris Hor, and Theresa DiMaio, Human Tumors Detected by Nuclear Magnetic Resonance, Proc Natl Acad Sci U S A. 1974 April; 71(4): 1471–1473.
- [10]. P. C. Lauterbur, Image Formation by Induced Local Interactions: Examples Employing Nuclear Magnetic Resonance, Nature, London, 242 (1973), pg. 190-191)
- [11]. Physiological Chemistry and Physics 9 (1977), pg 97-100,108
- [12]. Loeffler W, Oppelt A., Physical principles of NMR tomography. Eur J Radiol. 1981 Nov;1(4):338-44.

- [13]. Bradley WG, Shelden CH., Nuclear magnetic resonance imaging. Review of early clinical experience. *Am J Surg.* 1983 Jul;146(1):85-7.
- [14]. Go KG, van Dijk P et al. , Interpretation of nuclear magnetic resonance tomograms of the brain. *J Neurosurg.* 1983 Oct;59(4):574-84.
- [15]. Stejskal, E. O.; Tanner, J. E. (1 January 1965). "Spin Diffusion Measurements: Spin Echoes in the Presence of a Time-Dependent Field Gradient". *The Journal of Chemical Physics* 42 (1): 288.
- [16]. Le Bihan, D; E. Breton (1985). "Imagerie de diffusion in-vivo par résonance". *C R Acad Sci (Paris)* 301 (15): 1109–1112.
- [17]. Paul Tofts: *Quantitative MRI of the brain: measuring changes caused by disease.* ISBN: 0470847212
- [18]. Clarke GD, Lee Y. *The Principles of Quantitative MRI.* In *Advances in Medical Physics* 2008. ABWolbarst, KLMossman & WR Hendee, eds. (Medical Physics Publishing, Madison, WI) 2008.
- [19] Schwarcz A, Bogner P, Meric P, et al. The existence of biexponential signal decay in magnetic resonance diffusion-weighted imaging appears to be independent of compartmentalization. *Magn Reson Med* 2004;51(2):278—85.
- [20] Beuf O, Jaillon F, Saint-Jalmes H. Small-animal MRI: signal-to-noise ratio comparison at 7 and 1.5 T with multiple-animal acquisition strategies. *Magma* 2006;19(4):202—8.
- [21] Brockmann MA, Ulmer S, Leppert J, et al. Analysis of mouse brain using a clinical 1.5 T scanner and a standard small loop surface coil. *Brain Res* 2006;1068(1):138—42.
- [22] Chen F, De Keyser F, Wang H, et al. Diffusion weighted imaging in small rodents using clinical MRI scanners. *Methods* 2007;43(1):12—20.
- [23] Chen F, Suzuki Y, Nagai N, et al. Visualization of stroke with clinical MR imagers in rats: a feasibility study. *Radiology* 2004;233(3):905—11.

- [24] Chen F, Suzuki Y, Nagai N, Peeters R, Marchal G, Ni Y. Dynamic susceptibility contrast-enhanced perfusion MR imaging at 1.5 T predicts final infarct size in a rat stroke model. *J Neurosci Methods* 2005;141(1):55—60.
- [25] Guzman R, Lovblad KO, Meyer M, Spenger C, Schroth G, Widmer HR. Imaging the rat brain on a 1.5 T clinical MR-scanner. *J Neurosci Methods* 2000;97(1):77—85.
- [26] Lee FKF, Antonio GE, Yeung DK, Chan ET, Zhang LH, Yew DT, et al. Diffusion tensor imaging (DTI) of rodent brains in vivo using a 1.5 T clinical MR scanner. *J Magn Reson Imaging* 2006;23(5):747—51.
- [27] Linn J, Schwarz F, Schichor C, Wiesmann M. Cranial MRI of small rodents using a clinical MR scanner. *Methods* 2007;43(1):2—11.
- [28] Thorsen F, Ersland L, Nordli H, et al. Imaging of experimental rat gliomas using a clinical MR scanner. *J Neurooncol* 2003;63(3):225—31.
- [29] Ulmer S, Reeh M, Krause J, et al. Dynamic contrast-enhanced susceptibility-weighted perfusion MRI (DSC-MRI) in a glioma model of the rat brain using a conventional receive-only surface coil with a inner diameter of 47mm at a clinical 1.5 T scanner. *J Neurosci Methods* 2008;172(2):168—72.
- [30] Yang YM, Feng X, Yao ZW, Tang WJ, Liu HQ, Zhang L. Magnetic resonance angiography of carotid and cerebral arterial occlusion in rats using a clinical scanner. *J Neurosci Methods* 2008;167(2):176—83.
- [31] Sandner B, Pillai DR, Heidemann RM, et al. In vivo highresolution imaging of the injured rat spinal cord using a 3.0 T clinical MR scanner. *J Magn Reson Imaging* 2009;29(3):725—30.
- [32] Zhang S, He H, Lu W, Xu Q, Zhou B, Tang X. Tracking intrahepatically transplanted islets labeled with Feridexpolyethyleneimine complex using a clinical 3.0 T magnetic resonance imaging scanner. *Pancreas* 2009;38(3):293—302.

- [33] Daire JL, Jacob JP, Hyacinthe JN, et al. Cine and tagged cardiovascular magnetic resonance imaging in normal rat at 1.5 T: a rest and stress study. *J Cardiovasc Magn Reson* 2008;10(1):48.
- [34] Chang NK, Jeong YY, Park JS, et al. Tracking of neural stem cells in rats with intracerebral hemorrhage by the use of 3 T MRI. *Korean J Radiol* 2008;9(3):196—204.
- [35] Pinkernelle JG, Stelter L, Hamm B, Teichgräber U. Small animal MRI: clinical MRI as an interface to basic biomedical research. *Rofo* 2008;180(6):505—13.
- [36] Chen F, Suzuki Y, Nagai N, et al. Rodent stroke induced by photochemical occlusion of proximal middle cerebral artery: evolution monitored with MR imaging and histopathology. *Eur J Radiol* 2007;63(1):68—75.
- [37] Does MD, Gore JC. Compartmental study of T(1) and T(2) in rat brain and trigeminal nerve in vivo. *Magn Reson Med* 2002;47(2):274—83.
- [38] Hoehn-Berlage M, Eis M, Back T, Kohno K, Yamashita K. Changes of relaxation times (T1, T2) and apparent diffusion coefficient after permanent middle cerebral artery occlusion in the rat: temporal evolution, regional extent, and comparison with histology. *Magn Reson Med* 1995;34(6):824—34.
- [39] Stanisiz GJ, Odrobina EE, Pun J, et al. T1, T2 relaxation and magnetization transfer in tissue at 3T. *Magn Reson Med* 2005;54(3):507—12.
- [40] Lin SP, Schmidt RE, McKinstry RC, Ackerman JJ, Neil JJ. Investigation of mechanisms underlying transient T2 normalization in longitudinal studies of ischemic stroke. *J Magn Reson Imaging* 2002;15(2):130—6.
- [41] Schwarcz A, Berente Z, Osz E, Dóczy T. In vivo water quantification in mouse brain at 9.4 Tesla in a vasogenic edema model. *Magn Reson Med* 2001;46(6):1246—9.
- [42] Adalsteinsson E, Hurd RE, Mayer D, Sailasuta N, Sullivan EV, Pfefferbaum A. In vivo 2D J-resolved magnetic resonance spectroscopy of rat brain with a 3 T clinical human scanner.

Neuroimage 2004;22(1):381—6.

[43] Mayer D, Zahr NM, Sullivan EV, Pfefferbaum A. In vivo metabolite differences between the basal ganglia and cerebellum of the rat brain detected with proton MRS at 3 T. *Psychiatry Res* 2007;154(3):267—73.

[44] Mayer D, Zahr NM, Adalsteinsson E, Rutt B, Sullivan EV, Pfefferbaum A. In vivo fiber tracking in the rat brain on a clinical 3 T MRI system using a high strength insert gradient coil. *Neuroimage* 2007;35(3):1077—85.

[45] Pfefferbaum A, Adalsteinsson E, Sullivan EV. In vivo structural imaging of the rat brain with a 3 T clinical human scanner. *J Magn Reson Imaging* 2004;20(5):779—85.

[46] Liang ZPLP. Principles of magnetic resonance imaging: a signal processing perspective 2000:222—3.

[47] Kingsley P. Signal intensities and T1 calculations in multipleecho sequences with imperfect pulses. *Concepts Magn Reson* 1999;11:29—49.

[48] Kingsley PB, Ogg RJ, Reddick WE, Steen RG. Correction of errors caused by imperfect inversion pulses in MR imaging measurement of T1 relaxation times. *Magn Reson Imaging* 1998;16(9):1049—55.

[49] Natt O, Watanabe T, Boretius S, Radulovic J, Frahm J, Michaelis T. High-resolution 3D MRI of mouse brain reveals small cerebral structures in vivo. *J Neurosci Methods* 2002;120(2):203—9.

[50] Lin W, Venkatesan R, Gurleyik K, He YY, Powers WJ, Hsu CY. An absolute measurement of brain water content using magnetic resonance imaging in two focal cerebral ischemic rat models. *J Cereb Blood Flow Metab* 2000;20(1):37—44.

[51] Venkatesan R, Lin W, Gurleyik K, et al. Absolute measurements of water content using magnetic resonance imaging: preliminary findings in an in vivo focal ischemic rat model. *Magn Reson Med* 2000;43(1):146—50.

- [52] Barzo P, Marmarou A, Fatouros P, Hayasaki K, Corwin F. Contribution of vasogenic and cellular edema to traumatic brain swelling measured by diffusion-weighted imaging. *J Neurosurg* 1997;87(6):900—7.
- [53] Schwarcz A, Berente Z, Osz E, Dóczi T. Fast in vivo water quantification in rat brain oedema based on T(1) measurement at high magnetic field. *Acta Neurochir (Wien)* 2002;144(8), 811—815 discussion 815-816.
- [54] Vajda Z, Pedersen M, Doczi T, et al. Effects of centrally administered arginine vasopressin and atrial natriuretic peptide on the development of brain edema in hyponatremic rats. *Neurosurgery* 2001;49(3), 697—704; discussion 704-695.
- [55] An H, Lin W. Quantitative measurements of cerebral blood oxygen saturation using magnetic resonance imaging. *J Cereb Blood Flow Metab* 2000;20(8):1225—36.
- [56] Barbier EL, Liu L, Grillon E, et al. Focal brain ischemia in rat: acute changes in brain tissue T1 reflect acute increase in brain tissue water content. *NMR Biomed* 2005;18(8):499—506.
- [57] Calamante F, Lythgoe MF, Pell GS, et al. Early changes in water diffusion, perfusion, T1, and T2 during focal cerebral ischemia in the rat studied at 8.5 T. *Magn Reson Med* 1999;41(3):479—85.
- [58] de Graaf RA, Brown PB, McIntyre S, Nixon TW, Behar KL, Rothman DL. High magnetic field water and metabolite proton T1 and T2 relaxation in rat brain in vivo. *Magn Reson Med* 2006;56(2):386—94.
- [59] Del Bigio MR, Yan HJ, Kozlowski P, Sutherland GR, Peeling J. Serial magnetic resonance imaging of rat brain after induction of renal hypertension. *Stroke* 1999;30(11):2440—7.
- [60] Ewing JR, Jiang Q, Boska M, et al. T1 and magnetization transfer at 7 Tesla in acute ischemic infarct in the rat. *Magn Reson Med* 1999;41(4):696—705.
- [61] Gallez B, Demeure R, Baudalet C, et al. Non invasive quantification of manganese deposits in the rat brain by local measurement of NMR proton T1 relaxation times. *Neurotoxicology*

2001;22(3):387—92.

[62] Harris NG, Gauden V, Fraser PA, Williams SR, Parker GJ. MRI measurement of blood-brain barrier permeability following spontaneous reperfusion in the starch microsphere model of ischemia. *Magn Reson Imaging* 2002;20(3):221—30.

[63] Heiland S, Sartor K, Martin E, Bardenheuer HJ, Plaschke K. In vivo monitoring of age-related changes in rat brain using quantitative diffusion magnetic resonance imaging and magnetic resonance relaxometry. *Neurosci Lett* 2002;334(3):157—60.

[64] Kettunen MI, Grohn OH, Penttonen M, Kauppinen RA. Cerebral T1rho relaxation time increases immediately upon global ischemia in the rat independently of blood glucose and anoxic depolarization. *Magn Reson Med* 2001;46(3):565—72.

[65] Lei H, Zhang Y, Zhu XH, Chen W. Changes in the proton T2 relaxation times of cerebral water and metabolites during forebrain ischemia in rat at 9.4 T. *Magn Reson Med* 2003;49(6):979—84.

[66] Lythgoe MF, Thomas DL, Calamante F, et al. Acute changes in MRI diffusion, perfusion, T(1), and T(2) in a rat model of oligemia produced by partial occlusion of the middle cerebral artery. *Magn Reson Med* 2000;44(5):706—12.

[67] Plaschke K, Bardenheuer HJ, Martin E, Sartor K, Heiland S. Evolution of apparent diffusion coefficient and transverse relaxation time (T2) in the subchronic stage of global cerebral oligemia in different rat models. *Exp Brain Res* 2006;169(3):361—8.

[68] van Dorsten FA, Olah L, Schwandt W, et al. Dynamic changes of ADC, perfusion, and NMR relaxation parameters in transient focal ischemia of rat brain. *Magn Reson Med* 2002;47(1):97—104.

[69] Rooney WD, Johnson G, Li X, et al. Magnetic field and tissue dependencies of human brain longitudinal  $1\text{H}_2\text{O}$  relaxation in vivo. *Magn Reson Med* 2007;57(2):308—18.

[70] Kettunen MI, Grohn OH, Lukkarinen JA, Vainio P, Silvennoinen MJ, Kauppinen RA.

Interrelations of T(1) and diffusion of water in acute cerebral ischemia of the rat. *Magn Reson Med* 2000;44(6):833—9.

[71] Tofts PS, du Boulay EP. Towards quantitative measurements of relaxation times and other parameters in the brain. *Neuroradiology* 1990;32(5):407—15.

[72] Niendorf T, Dijkhuizen RM, Norris DG, van Lookeren Campagne M, Nicolay K. Biexponential diffusion attenuation in various states of brain tissue: implications for diffusion-weighted imaging. *Magn Reson Med* 1996;36(6):847—57.

[73] Schwarcz A, Ursprung Z, Berente Z, et al. In vivo brain edema classification: New insight offered by large b-value diffusionweighted MR imaging. *J Magn Reson Imaging* 2007;25(1): 26—31.

[74] Dong Z, Dreher W, Leibfritz D. Toward quantitative shortecho-time in vivo proton MR spectroscopy without water suppression. *Magn Reson Med* 2006;55(6):1441—6.

[75] Pfeuffer JTI, Provencher SW, Gruetter R. Toward an in vivo neurochemical profile: quantification of 18 metabolites in short-echo-time (1)H NMR spectra of the rat brain. *J Magn Reson* 1999;141(1):104—20.

[76] Schwarcz A, Natt O, Watanabe T, Boretius S, Frahm J, Michaelis T. Localized proton MRS of cerebral metabolite profiles in different mouse strains. *Magn Reson Med* 2003;49(5):822—7.

[77]. Headache Classification Committee of the International Headache Society. The International Classification of Headache Disorders, 2nd edn. *Cephalalgia*. 2004;24(Suppl. 1):1-160.

[78]. Kruit MC, van Buchem MA, Hofman PA, et al. Migraine is a risk factor for subclinical brain lesions. *JAMA*. 2004;291:427-434.

[79]. Kruit MC, Launer LJ, Ferrari MD, van Buchem MA. Infarcts in the posterior circulation territory in migraine. The population-based MRI CAMERA study. *Brain*. 2005;128:2068-2077.

[80]. Kruit MC, Launer LJ, Ferrari MD, van Buchem MA. Brain stem and cerebellar hyperintense

lesions in migraine. *Stroke*. 2006;37:1109-1112.

[81]. Kruit MC, van Buchem MA, Launer LJ, Terwindt GM, Ferrari MD. Migraine is associated with an 10 increased risk of deep white matter lesions, subclinical posterior circulation infarcts and brain iron accumulations: The population-based MRI CAMERA study. *Cephalalgia*. 2010;30:129-136.

[82]. Kurth T, Mohamed S, Maillard P, et al. Headache, migraine, and structural brain lesions and function: Population based Epidemiology of Vascular Ageing- MRI study. *BMJ*. 2011;342:c7357.

[83]. Swartz RH, Kern RZ. Migraine is associated with magnetic resonance imaging white matter abnormalities: A meta-analysis. *Arch Neurol*. 2004;61: 1366-1368.

[84]. Fazekas F, Koch M, Schmidt R, et al. The prevalence of cerebral damage varies with migraine type: A MRI study. *Headache*. 1992;32:287-291.

[85]. De Benedittis G, Lorenzetti A, Sina C, Bernasconi V. Magnetic resonance imaging in migraine and tension-type headache. *Headache*. 1995;35:264-268.

[86]. Schmitz N, Admiraal-Behloul F, Arkink EB, et al. Attack frequency and disease duration as indicators for brain damage in migraine. *Headache*. 2008;48:1044-1055.

[87]. Trauninger A, Leél-Ossy E, Kamson DO, et al. Risk factors of migraine-related brain white matter hyperintensities: An investigation of 186 patients. *J Headache Pain*. 2011;12:97-103.

[88]. Bednarczyk EM, Remler B, Weikart C, Nelson AD, Reed RC. Global cerebral blood flow, blood volume, and oxygen metabolism in patients with migraine headache. *Neurology*. 1998;50:1736-1740.

[89]. Rocca MA, Colombo B, Inglese M, Codella M, Comi G, Filippi M. A diffusion tensor magnetic resonance imaging study of brain tissue from patients with migraine. *J Neurol Neurosurg Psychiatry*. 2003;74:501-503.

- [90]. Valfrè W, Rainero I, Bergui M, Pinessi L. Voxelbased morphometry reveals gray matter abnormalities in migraine. *Headache*. 2008;48:109-117.
- [91]. Cutrer FM, Black DF. Imaging findings of migraine. *Headache*. 2006;46:1095-1107.
- [92]. Gouw AA, Seewann A, van der Flier WM, et al. Heterogeneity of small vessel disease: A systematic review of MRI and histopathology correlations. *J Neurol Neurosurg Psychiatry*. 2011;82:126-135.
- [93]. Filippi M, Rocca MA, Barkhof F, et al.; Attendees of the Correlation between Pathological MRI Findings in MS Workshop. Association between pathological and MRI findings in multiple sclerosis. *Lancet Neurol*. 2012;11:349-360.
- [94]. Hoque R, Ledbetter C, Gonzalez-Toledo E, et al. The role of quantitative neuroimaging indices in the differentiation of ischemia from demyelination: An analytical study with case presentation. *Int Rev Neurobiol*. 2007;79:491-519.
- [95]. Zivadinov R, Bergsland N, Stosic M, et al. Use of perfusion- and diffusion-weighted imaging in differential diagnosis of acute and chronic ischemic stroke and multiple sclerosis. *Neurol Res*. 2008;30:816-826.
- [96]. Vermeer SE, Hollander M, van Dijk EJ, Hofman A, Koudstaal PJ, Breteler MMB. Silent brain infarcts and white matter lesions increase stroke risk in general population. *Stroke*. 2003;34:1126-1129.
- [97]. Provencher SW. Automatic quantitation of localized in vivo <sup>1</sup>H spectra with LCModel. *NMR Biomed*. 2001;14:260-264.
- [98]. Pagani E, Bizzi A, Di Salle F, De Stefano N, Filippi M. Basic concepts of advanced MRI techniques. *Neurol Sci*. 2008;29:S290-S295.
- [99]. Lancaster JL, Andrews T, Hardies LJ, Dodd S, Fox PT. Three-pool model of white matter. *J Magn Reson Imaging*. 2003;17:1-10.
- [100]. Zhu YC, Dufouil C, Tzourio C, Chabriat H. Silent brain infarcts: A review of MRI

diagnostic criteria. *Stroke*. 2011;42:1140-1145.

[101]. Schwarcz A, Ursprung Z, Berente Z, et al. In vivo brain edema classification: New insight offered by large b-value diffusion-weighted MR imaging. *J Magn Reson Imaging*. 2007;25:26-31.

[102]. Moore GJ. Proton magnetic resonance spectroscopy in pediatric neuroradiology. *Pediatr Radiol*. 1998;28: 805-814.

[103]. Barkhof F, van Walderveen M. Characterization of tissue damage in multiple sclerosis by nuclear magnetic resonance. *PhilosTrans R Soc Lond B Biol Sci*. 1999;354:1675-1686.

[104]. Mader I, Rauer S, Gall P, Klose U. <sup>1</sup>H MR spectroscopy of inflammation, infection and ischemia of the brain. *Eur J Radiol*. 2008;67:250-257.

[105]. Rumpel H, Lim WE, Chang HM, et al. Is myoinositol a measure of glial swelling after stroke? A magnetic resonance study. *J Magn Reson Imaging*. 2003;17:11-19.

[106]. Wuerfel J, Bellmann-Strobl J, Brunecker P, et al. Changes in cerebral perfusion precede plaque formation in multiple sclerosis: A longitudinal perfusion MRI study. *Brain*. 2004;127:111-119. *Headache* 11

[107]. Helms G. Volume correction for edema in single-volume proton MR spectroscopy of contrast-enhancing multiple sclerosis lesions. *Magn Reson Med*. 2001;46:256-263.

[108]. Bakshi R, Thompson AJ, Rocca MA, et al. MRI in multiple sclerosis: Current status and future prospects. *Lancet Neurol*. 2008;7:615-625.

[109]. Walker PM, Ben Salem D, Lalande A, Giroud M, Brunotte F. Time course of NAAT2 and ADC(w) in ischaemic stroke patients: <sup>1</sup>H MRS imaging and diffusion-weighted MRI. *J Neurol Sci*. 2004;220:23-28.

[110]. Barber PA, Consolo HK, Yang Q, et al. Comparison of MRI perfusion imaging and single photon emission computed tomography in chronic stroke. *Cerebrovasc Dis*. 2001;11:128-136.

[111]. Saunders DE. MR spectroscopy in stroke. *Br Med Bull*. 2000;56:334-345.

- [112]. Oppenheimer SM, Bryan RN, Conturo TE, Soher BJ, Preziosi TJ, Barker PB. Proton magnetic resonance spectroscopy and gadolinium-DTPA perfusion imaging of asymptomatic MRI white matter lesions. *Magn Reson Med*. 1995;33:61-68.
- [113]. Sappey-Marini D, Calabrese G, Hetherington HP, et al. Proton magnetic resonance spectroscopy of human brain: Applications to normal white matter, chronic infarction, and MRI white matter signal hyperintensities. *Magn Reson Med*. 1992;26:313-327.
- [114]. Cutrer FM, Sorensen AG, Weisskoff RM, et al. Perfusion-weighted imaging defects during spontaneous migrainous aura. *Ann Neurol*. 1998;43:25-31.
- [115]. Sanchez del Rio M, Bakker D, Wu O, et al. Perfusion weighted imaging during migraine: Spontaneous visual aura and headache. *Cephalalgia*. 1999;19:701-707.
- [116]. Gursoy-Ozdemir Y, Qiu J, Matsuoka N, et al. Cortical spreading depression activates and upregulates MMP-9. *J Clin Invest*. 2004;113:1447-1455.
- [117]. Milhaud D, Bogousslavsky J, van Melle G, Liot P. Ischemic stroke and active migraine. *Neurology*. 2001;57:1805-1811.
- [118]. Tietjen GE, Herial NA, White L, Utley C, Kosmyna JM, Khuder SA. Migraine and biomarkers of endothelial activation in young women. *Stroke*. 2009;40: 2977-2982.
- [119]. Uzar E, Evliyaoglu O, Toprak G, et al. Increased asymmetric dimethylarginine and nitric oxide levels in patients with migraine. *J Headache Pain*. 2011;12: 239-243.
- [120]. Singhal AB, Hajj-Ali RA, Topcuoglu MA, et al. Reversible cerebral vasoconstriction syndromes: Analysis of 139 cases. *Arch Neurol*. 2011;68:1005-1012.
- [121] Sellner J, Boggild M, Clanet M, Hintzen RQ, Illes Z, Montalban X, Du Pasquier RA, Polman CH, Sorensen PS, Hemmer B: EFNS guidelines on diagnosis and management of neuromyelitis optica. *Eur J Neurol* 2010; 17: 1019–1032.
- [122] Yu CS, Lin FC, Li KC, Jiang TZ, Zhu CZ, Qin W, Sun H, Chan P: Diffusion tensor imaging in the assessment of normal-appearing brain tissue damage in relapsing neuromyelitis

optica. *Am J Neuroradiol* 2006; 27: 1009–1015.

[123] Bichuetti DB, Rivero RL, de Oliveira EM, Oliveira DM, de Souza NA, Nogueira RG, Abdala N, Gabbai A: White matter spectroscopy in neuromyelitis optica: a case control study. *J Neurol* 2008; 255: 1895–1899.

[124] de Seze J, Blanc F, Kremer S, Collongues N, Fleury M, Marcel C, Namer IJ: Magnetic resonance spectroscopy evaluation in patients with neuromyelitis optica. *J Neurol Neurosurg Psychiatry* 2010; 81: 409–411.

[125] Schwarcz A, Ursprung Z, Berente Z, Bogner P, Kotek G, Méric P, Gillet B, Beloeil JC, Dóczi T: In vivo brain edema classification: new insight offered by large b-value diffusion weighted MR imaging. *J Magn Reson Imaging* 2007; 25: 26–31.